



1
2
3 **Satellite observations of atmospheric methane**
4 **and their value for quantifying methane emissions**

5 Daniel J. Jacob (djacob@fas.harvard.edu)¹, Alexander J. Turner¹, Joannes D. Maasakkers¹,
6 Jianxiong Sheng¹, Kang Sun², Xiong Liu², Kelly Chance², Ilse Aben³, Jason McKeever⁴,
7 Christian Frankenberg⁵

8
9 ¹School of Engineering and Applied Sciences, Harvard University, Cambridge, Massachusetts
10 USA

11 ² Smithsonian Astrophysical Observatory, Cambridge, Massachusetts USA

12 ³ SRON Netherlands Institute for Space Research, Utrecht, Netherlands

13 ⁴ GHGSat, Inc., Montreal, Canada

14 ⁵ California Institute of Technology, Pasadena, California USA

15
16 submitted to *Atmospheric Chemistry and Physics*

17
18 June 24, 2016

19
20 **Abstract**

21
22 Methane is a greenhouse gas emitted by a range of natural and anthropogenic sources.
23 Atmospheric methane has been measured continuously from space since 2003, and new
24 instruments are planned for launch in the near future that will greatly expand the capabilities of
25 space-based observations. We review the value of current, future, and proposed satellite
26 observations to better quantify and understand methane emissions through inverse analyses,
27 down to the scale of point sources and in combination with suborbital (surface and aircraft) data.
28 Current observations from GOSAT are of high quality but have sparse spatial coverage. They
29 provide limited information to quantify methane emissions on a regional (100-1000 km) scale.
30 TROPOMI to be launched in late 2016 is expected to quantify daily emissions on the regional
31 scale and will also effectively detect large point sources. Future satellite instruments with much
32 higher spatial resolution, such as the recently launched GHGSat with 50×50 m² resolution over
33 targeted viewing domains, have the potential to detect a wide range of methane point sources.
34 Geostationary observation of methane, still in the proposal stage, will have unique capability for
35 mapping source regions with high resolution while also detecting transient “super-emitter” point
36 sources. Exploiting the rapidly expanding satellite measurement capabilities to quantify methane
37 emissions requires a parallel effort to construct high-quality spatially and sectorally resolved
38 emission inventories. Partnership between top-down inverse analyses of atmospheric data and
39 bottom-up construction of emission inventories is crucial to better understand methane emission
40 processes and from there to inform climate policy.

41
42



43 1. Introduction

44

45

46 Methane is a greenhouse gas emitted by anthropogenic sources including livestock,
47 oil/gas systems, landfills, coal mines, wastewater management, and rice cultivation. Wetlands are
48 the dominant natural source. The atmospheric concentration of methane has risen from 720 to
49 1800 ppb since pre-industrial times (Hartmann et al., 2013). The resulting radiative forcing on an
50 emission basis is 0.97 W m^{-2} , compared to 1.68 W m^{-2} for CO_2 (Myhre et al., 2013). The present-
51 day global emission of methane is well-known to be $550 \pm 60 \text{ Tg a}^{-1}$, as inferred from mass
52 balance with the global methane sink from oxidation by OH radicals (Prather et al., 2012).
53 However, the contributions from different source sectors and source regions are highly uncertain
54 (Dlugokencky et al., 2011; Kirschke et al., 2013). Emission inventories used for climate policy
55 rely on “bottom-up” estimates of activity rates and emission factors for individual source
56 processes. “Top-down” information from observations of atmospheric methane is often at odds
57 with these estimates (Brandt et al., 2014). Satellite observations of atmospheric concentrations
58 have emerged over the past decade as a promising resource to monitor emissions of various
59 gases (Streets et al., 2013). Here we review present, near-future, and proposed satellite
60 observations of atmospheric methane and assess their value for quantifying emissions, down to
61 the scale of individual point sources.

61

62 The United Nations Framework Convention on Climate Change (UNFCCC) requires
63 individual countries to report their annual national greenhouse gas emissions following bottom-
64 up inventory guidelines from the International Panel on Climate Change (IPCC, 2006). The 2015
65 Paris Agreement further requires countries to develop plans for reducing greenhouse gas
66 emissions. Reducing methane emissions is a major target of US climate policy (President’s
67 Action Plan, 2014). Figure 1 shows the US anthropogenic methane emission inventory for 2012
68 compiled by the Environmental Protection Agency (EPA, 2016) and reported to the UNFCCC.
69 The inventory uses advanced IPCC Tier 2/3 methods (IPCC, 2006) and provides detailed sector
70 information. However, atmospheric observations from surface sites and aircraft suggest that US
71 emissions are about 50% higher, and that sources from natural gas and livestock are likely
72 responsible for the underestimate (Miller et al., 2013; Brandt et al., 2014). Emissions from
73 natural gas can take place at all points along the supply chain from production to distribution. A
74 small population of highly-emitting sources (the so-called “super-emitters”) associated with
75 faulty equipment or episodic venting may contribute disproportionately to total emissions
76 (Marchese et al., 2015; Mitchell et al., 2015; Zavala-Araiza et al., 2015).

76

77 Atmospheric observations offer a test of emission inventories. Targeted local
78 measurements of atmospheric methane can quantify emissions on small scales (point source,
79 urban area, oil/gas basin) by measuring the ratio of methane to a co-emitted species whose
80 emission is known (Wennberg et al., 2012) or by using a simple mass balance approach (Karion
81 et al., 2013, 2015; Peischl et al., 2013, 2016; Conley et al., 2016). Quantifying emissions on
82 larger scales, with many contributing sources, requires a more general approach where an
83 ensemble of atmospheric observations is fit to a 2-D field of emissions by inversion of a 3-D
84 chemical transport model (CTM) that relates emissions to atmospheric concentrations. This
85 inversion is usually done by Bayesian optimization accounting for errors in the CTM, in the
86 observations, and in the prior knowledge expressed by the bottom-up inventory. We obtain from
87 the inversion a statistically optimized emission field, and differences with the bottom-up
88 inventory point to areas where better understanding of processes is needed. A large number of
inverse studies have used surface and aircraft observations to quantify methane emissions on



89 regional to global scales (Bergamaschi et al., 2005; Bousquet et al., 2011; Miller et al., 2013;
90 Bruhwiler et al., 2014).
91 Satellites provide global, dense, and continuous data that are particularly well suited for
92 inverse analyses. Measurement of methane from space began with the IMG thermal infrared
93 instrument in 1996-1997 (Clerbaux et al., 2003). Measurement of total methane columns by solar
94 backscatter began with SCIAMACHY in 2003-2012 (Frankenberg et al., 2006) and continues to
95 the present with GOSAT launched in 2009 (Kuze et al., 2016). Satellite measurements of
96 atmospheric methane have been used to detect emission hotspots (Worden et al., 2012; Kort et
97 al., 2014; Marais et al., 2014) and to estimate emission trends (Schneising et al., 2014; Turner et
98 al., 2016). They have been used in global inverse analyses to estimate emissions on regional
99 scales (Bergamaschi et al., 2007, 2009, 2013; Monteil et al., 2013; Cressot et al., 2014; Wecht et
100 al., 2014a; Alexe et al., 2015; Turner et al., 2015). The TROPOMI instrument scheduled for
101 launch in late 2016 will vastly expand the capability to observe methane from space by providing
102 complete daily global coverage with $7 \times 7 \text{ km}^2$ resolution (Veefkind et al., 2012; Butz et al.,
103 2012). The GHGSat instrument launched on a microsatellite in June 2016 by a private company
104 (GHGSat, Inc.) has $50 \times 50 \text{ m}^2$ pixel resolution over targeted viewing domains that may allow
105 detection of a wide range of methane point sources. GOSAT-2, a successor of GOSAT featuring
106 higher precision, is scheduled for launch in 2018. Additional instruments are in the planned or
107 proposed stage. As the demand for global monitoring of methane emissions grows, it is timely to
108 review the capabilities and limitations of present and future satellite observations.

110 2. Observing methane from space

111 2.1 Instruments and retrievals

112 Table 1 list the principal instruments (past, current, planned, proposed) measuring
113 methane from space. Atmospheric methane is detectable by its absorption of radiation in the
114 shortwave infrared (SWIR) at 1.65 and 2.3 μm , and in the thermal infrared (TIR) around 8 μm .
115 Figure 2 shows different satellite instrument configurations. SWIR instruments measure solar
116 radiation backscattered by the Earth and its atmosphere. The MERLIN lidar instrument will emit
117 its own SWIR radiation and detect methane in the back-scattered laser signal. TIR instruments
118 measure blackbody terrestrial radiation absorbed and re-emitted by the atmosphere. They can
119 operate in the nadir as shown in Fig. 2, measuring upwelling radiation, or in the limb by
120 measuring slantwise through the atmosphere. Solar occultation instruments (not shown in Fig. 2)
121 stare at the Sun through the atmosphere as the orbiting satellite experiences sunrises and sunsets.
122 Limb and solar occultation instruments detect methane in the stratosphere and upper troposphere,
123 but not at lower altitudes because of cloud interferences. They are not listed in Table 1 but are
124 referenced in Sect. 3.2 for measuring stratospheric methane.

125 All instruments launched to date have been in polar sun-synchronous low Earth orbit
126 (LEO), circling the globe at fixed local times of day. They detect methane in the nadir along the
127 orbit track, and most also observe off-nadir (at a cross-track angle) for additional coverage.
128 Unlike other instruments, GHGSat focuses not on global coverage but on specific targets with
129 very fine pixel resolution and limited viewing domains. Geostationary instruments still at the
130 proposal stage would allow a combination of high spatial and temporal resolution over
131 continental-scale domains, and could observe either in the SWIR or in the TIR following the
132 configurations of Fig. 2.



133 Figure 3 shows typical vertical sensitivities for instruments in the SWIR and TIR.
 134 Instrument sensitivity extending down to the surface is desirable to infer methane emissions.
 135 This is achieved in the SWIR, where the atmosphere is nearly transparent unless clouds are
 136 present (Frankenberg et al., 2005). SWIR instruments thus measure the total atmospheric column
 137 of methane, with no vertical resolution. Measurements in the TIR require a thermal difference
 138 between the atmosphere and the surface (T_l vs. T_o in Fig. 2) and this limits their sensitivity to the
 139 middle and upper troposphere.

140 Figure 4 shows the atmospheric optical depths of different gases in the SWIR,
 141 highlighting the methane absorption bands at 1.65 μm and 2.3 μm . All solar backscatter
 142 instruments so far have operated at 1.65 μm but TROPOMI will operate at 2.3 μm . GOSAT-2
 143 will operate at both. SCIAMACHY was intended to operate at 2.3 μm and some retrievals were
 144 done in that band (GlouDEMANS et al., 2008) but an ice layer on the detector decreased
 145 performance and the operational retrievals were done at 1.65 μm instead. The 2.3 μm band is
 146 stronger, as shown in Fig. 3, and also allows retrieval of carbon monoxide (CO) which is of
 147 interest as an air pollutant and tracer of transport (Worden et al., 2010). However, solar radiation
 148 is 3 times weaker at 2.3 than at 1.65 μm . The 1.65 μm band has the advantage that CO₂ can also
 149 be retrieved, which greatly facilitates the methane retrieval as described below.

150 Methane retrievals at either 1.65 or 2.3 μm fit the reflected solar spectrum measured by
 151 the satellite to a modeled spectrum in order to derive the total vertical column density Ω
 152 [molecules cm^{-2}] of methane, taking into account the viewing geometry and often including a
 153 prior estimate to regularize the retrieval (Frankenberg et al., 2006; Schepers et al., 2012):
 154

$$155 \quad \hat{\Omega} = \Omega_A + \mathbf{a}^T (\boldsymbol{\omega} - \boldsymbol{\omega}_A) \quad (1)$$

156
 157 Here $\hat{\Omega}$ is the retrieved vertical column density, Ω_A is the prior best estimate assumed in the
 158 retrieval, $\boldsymbol{\omega}_A$ is a vector of prior estimates of partial columns [molecules cm^{-2}] at successive
 159 altitudes summing up to Ω_A , and $\boldsymbol{\omega}$ is the vector of true values for these partial columns. The
 160 column averaging kernel vector \mathbf{a} expresses the sensitivity of the measurement as a function of
 161 altitude (Fig. 3), and is the reduced expression of an averaging kernel matrix that describes the
 162 ability of the retrieval to fit not only $\boldsymbol{\omega}$ but other atmospheric and spectroscopic variables as well
 163 (Frankenberg et al., 2005; Schepers et al., 2012). The elements of \mathbf{a} have values near unity
 164 through the depth of the troposphere at either 1.65 or 2.3 μm , meaning that SWIR instruments
 165 are sensitive to the full column of methane and that the prior estimates do not contribute
 166 significantly to the retrieved columns.

167 The viewing geometry of the satellite measurement is defined by the solar zenith angle θ
 168 and the satellite viewing angle θ_v (Fig. 2). This defines a geometric air mass factor ($\cos^{-1}\theta + \cos^{-1}\theta_v$)
 169 for the slant column path of the solar radiation propagating through the atmosphere and
 170 reflected to the satellite. Division by this air mass factor converts the slant column obtained by
 171 fitting the backscattered spectrum to the actual vertical column, assuming that the incident and
 172 reflected solar beams sample the same methane concentrations. This assumption is safe for pixel
 173 sizes larger than 1 km but breaks down when observing methane plumes at smaller pixel sizes, as
 174 discussed in Sect. 4.

175 The methane vertical column density Ω is sensitive to changes in surface pressure from
 176 topography and weather, affecting the total amount of air in the column. This dependence can be
 177 removed by converting Ω to a dry-air column-average mole fraction $X = \Omega/\Omega_a$ (also called



178 column-average mixing ratio) where Ω_a is the vertical column density of dry air as determined
179 from the local surface pressure and humidity. X is a preferred measure of the methane
180 concentration because it is insensitive to changes in pressure and humidity.

181 Solar backscatter measurements in the SWIR require a reflective surface. This largely
182 limits the measurements to land, although some ocean data can be obtained from specular
183 reflection at the ocean surface (sunglint). Clouds interfere with the measurement, reflecting solar
184 radiation back to space and preventing detection of the air below the cloud while also affecting
185 the accuracy of the retrievals. Even partly cloudy scenes are problematic because the radiation
186 from the highly reflective cloudy fraction contributes disproportionately to the total
187 backscattered radiation from the pixel. An important advantage of finer pixel resolution is to
188 increase the probability of clear-sky scenes (Remer et al., 2012). The GOSAT retrievals exclude
189 cloudy scenes by using a simultaneous retrieval of the oxygen column in the $0.76 \mu\text{m}$ A-band. A
190 low oxygen column indicates the presence of cloud. For SCIAMACHY this is impractical
191 because the pixel resolution is so coarse ($30 \times 60 \text{ km}^2$) that a clear-sky requirement would exclude
192 too much data; instead the retrieval allows for partly cloudy scenes (Frankenberg et al., 2006).
193 The fraction of successful retrievals is 17% for GOSAT (Parker et al. (2011) retrieval) and 9%
194 for SCIAMACHY (Frankenberg et al. (2011) retrieval), largely limited by cloud cover.
195 TROPOMI retrievals will exclude cloudy scenes by using cloud observations from the VIIRS
196 solar backscatter instrument flying in formation and viewing the same scenes at fine pixel
197 resolution (Veefkind et al., 2012).

198 Two different methods have been used for methane retrievals at $1.65 \mu\text{m}$ (SCIAMACHY,
199 GOSAT): the CO_2 proxy method (Frankenberg et al., 2005) and the full-physics method (Butz et
200 al., 2010). In the full-physics method, the scattering properties of the surface and the atmosphere
201 are fitted as part of the retrieval, using additional fitting variables to describe the scattering. In
202 the CO_2 proxy method, the spectral fit for methane ignores atmospheric scattering, and the
203 resulting methane column is subsequently corrected for scattering by using a separate retrieval of
204 CO_2 (also ignoring atmospheric scattering) in its nearby $1.6 \mu\text{m}$ absorption band as shown in Fig.
205 4. This assumes that atmospheric scattering affects the light paths for methane and CO_2 retrievals
206 in the same way (since the wavelengths are nearby and absorption strengths are similar). It also
207 assumes that the dry-air column mole fraction of CO_2 is known (it is far less variable than for
208 methane). The dry-air column mole fraction of methane is then obtained by scaling to the CO_2
209 retrieval:

210

$$211 \quad X_{CH_4} = \left(\frac{\Omega_{CH_4}}{\Omega_{CO_2}} \right) X_{CO_2} \quad (2)$$

212

213 Here X_{CO_2} is taken from independent information such as the CarbonTracker data assimilation
214 product (Peters et al., 2007) or a multi-model ensemble (Parker et al., 2015). An advantage of the
215 CO_2 proxy method is that it corrects for instrument biases affecting both methane and CO_2 . A
216 drawback is that errors in X_{CO_2} propagate to X_{CH_4} . Comparisons of retrievals using the full-
217 physics and CO_2 proxy methods show that they are of comparable quality (Buchwitz et al., 2015)
218 but the CO_2 proxy method is much more computationally efficient (Schepers et al., 2012). The
219 CO_2 proxy method can be problematic for methane plumes with joint enhancements of CO_2 ,
220 such as from megacities or open fires, that would not be resolved in the independent information
221 for X_{CO_2} .



222 Figure 5 shows the global and US distributions of methane (X_{CH_4}) observed by
223 SCIAMACHY (2003-2004) and GOSAT (2010-2013). We focus on 2003-2004 for
224 SCIAMACHY because of radiation-induced detector degradation after 2005 (Kleipool et al.,
225 2007). Global methane concentrations increased by 30 ppb from 2003-2004 to 2010-2013
226 (Hartmann et al., 2013), and the colorscale in Fig. 5 is correspondingly shifted to facilitate
227 pattern comparisons. Observations are mainly restricted to land but GOSAT also observes
228 sunglint over the oceans. SCIAMACHY provides full global mapping, while GOSAT observes
229 only at selected pixel locations leaving gaps between pixels. Low values of X_{CH_4} over elevated
230 terrain (Greenland, Himalayas, US Intermountain West) reflect a larger relative contribution of
231 the stratosphere (with lower methane) to the total atmospheric column. SCIAMACHY has
232 positive biases over the Sahara and at high latitudes (Sect. 2.2).

233 The SCIAMACHY and GOSAT global distributions show commonality in patterns.
234 Values are highest in East Asia, consistent with the Emissions Database for Global Atmospheric
235 Research (EDGAR) inventory (European Commission, 2011), where the dominant contributions
236 are from rice cultivation, livestock, and coal mining. Values are also high over central Africa and
237 northern South America because of wetlands and livestock. Over the US, both SCIAMACHY
238 and GOSAT feature high values in the South-Central US (oil/gas, livestock) and hotspots in the
239 Central Valley of California and in eastern North Carolina (livestock). There are also high values
240 in the Midwest that are less consistent between the two sensors and might reflect a combination
241 of oil/gas, livestock, and coal mining sources.

242 TROPOMI will observe methane in the 2.3 μm band in order to also retrieve CO. The
243 proposed geostationary instruments of Table 1 also target the 2.3 μm band in order to track CO
244 plumes. Retrieval at 2.3 μm does not allow the CO₂ proxy method because no neighboring CO₂
245 band is available in that part of the spectrum (Fig. 4). Retrievals of methane from TROPOMI
246 will therefore rely on the full-physics method. The operational retrieval for TROPOMI is
247 described by Butz et al. (2012), who find that the precision error is almost always better than 1%
248 and that over 90% of cloud-free scenes can be successfully retrieved. Observations of methane-
249 CO correlations from joint 2.3 μm retrievals may provide useful additional information for
250 inferring methane sources (Xiao et al., 2004; Wang et al., 2009; Worden et al., 2013).

251 Observations of methane in the TIR are available from the IMG, AIRS, TES, IASI, and
252 CrIS instruments (Table 1). These instruments observe the temperature-dependent blackbody
253 radiation emitted by the Earth and its atmosphere. Atmospheric methane absorbs upwelling
254 radiation in a number of bands around 8 μm and re-emits it at a colder temperature. The methane
255 concentration is retrieved from the temperature contrast. TIR instruments have little sensitivity to
256 the lower troposphere because of insufficient temperature contrast with the surface, as illustrated
257 in Fig. 3. This makes them less useful for detecting local/regional methane emissions. On the
258 other hand, they observe both day and night, over land and ocean, and provide concurrent
259 retrievals of other trace gases that can be correlated with methane such as CO and ammonia.
260 Worden et al. (2013) showed that TIR measurements can be particularly effective at quantifying
261 methane emissions from open fires, because aerosol interference is negligible in the TIR and
262 concurrent retrieval of CO allows inference of the methane/CO emission factor.

263 Multispectral retrievals in the SWIR and TIR combine the advantages of both approaches
264 and provide some vertical profile information, as demonstrated by Herbin et al. (2013) using the
265 combination of SWIR and TIR data from GOSAT, and by Worden et al. (2015) using the
266 combination of SWIR from GOSAT and TIR from TES. This could enable separation between
267 the local/regional methane enhancement near the surface and the higher-altitude methane



268 background (Bousserez et al., 2015). Such multi-spectral retrievals are not yet produced
269 operationally because of computational requirements and because of limitations in the quality
270 and calibration of spectra across different detectors (Hervé Herbin, personal communication).

271 The MERLIN lidar instrument scheduled for launch in 2020 (Kiemle et al., 2011) will
272 measure methane in the pencil of 1.65 μm radiation emitted by a laser along the satellite track
273 and reflected directly back to the satellite. It will observe the full vertical column of methane
274 during day and night, over both land and oceans, and will have unique capability for observing
275 high latitudes during the dark season. By measuring only the direct reflected radiation it will not
276 be affected by scattering errors, unlike the passive SWIR instruments, and cloud interferences
277 will be minimized. Kiemle et al. (2014) show that monthly and spatial averaging of the
278 MERLIN data on a $50 \times 50 \text{ km}^2$ grid should provide global mapping of methane concentrations
279 with 1% precision.

280 Other instruments in Table 1 are presently at the proposal stage. All use solar backscatter.
281 CarbonSat (Buchwitz et al., 2013) is designed to measure methane globally with an
282 unprecedented combination of fine pixel resolution ($2 \times 2 \text{ km}^2$) and high precision (0.4%). It was
283 a finalist for the ESA's Earth Explorer Program in 2015 but was not selected. GEO-CAPE
284 (Fishman et al., 2012), GeoFITS (Xi et al., 2015), and geoCARB (Polonsky et al., 2014) are
285 geostationary instruments for methane that have been proposed to NASA but so far without
286 success. Geostationary capabilities are discussed further in Sect. 4.

287

288 **2.2 Error characterization**

289 Satellite observations require careful error characterization for use in inverse analyses.
290 Errors may arise from light collection by the instrument, dark current, spectroscopic data, the
291 radiative transfer model, cloud contamination, and other factors. Kuze et al. (2016) give a
292 detailed description of GOSAT instrument errors as informed by 5 years of operation. Errors
293 may be random, such as from photon count statistics, or systematic, such as from inaccurate
294 spectroscopic data. They may increase with time due to instrument degradation.

295 Random error (precision) and systematic error (accuracy) have very different impacts
296 (Kulawik et al., 2016). Random error can be reduced by repeated observations and averaging. As
297 we will illustrate in Sect. 4, instrument precision can define the extent of spatial/temporal
298 averaging required for satellite observations to usefully quantify emissions. Systematic error, on
299 the other hand, is irreducible and propagates in the inversion to cause a corresponding bias in the
300 emission estimates. A uniform global bias is not problematic for methane since the global mean
301 concentration is well known from surface observations, but a spatially variable bias affects
302 source attribution by aliasing the methane enhancements relative to background. Buchwitz et al.
303 (2015) refer to this spatial variability in the bias as "relative bias". It can arise for example from
304 different surface reflectivities, aerosol interference, sloping terrain, or unresolved variability in
305 CO_2 columns when using the CO_2 proxy method (Schepers et al., 2012; Alexe et al., 2015).
306 Buchwitz et al. (2015) estimate threshold requirements of 34 ppb single-observation precision
307 and 10 ppb relative bias for solar backscatter satellite observations to be useful in inversions of
308 methane emissions on regional scales.

309 Validation of satellite data requires highly accurate suborbital observations of methane
310 from surface sites, aircraft, or balloons. Direct validation involves comparison of single-scene
311 satellite retrievals to suborbital observations of that same scene. The suborbital observations
312 must be collocated in space and time with the satellite overpass, and they must provide a full
313 characterization of the column as observed by the satellite. Although direct validation is by far



314 the preferred means of validation, the requirements greatly limit the conditions under which it
315 can be done. Indirect validation is a complementary method that involves diagnosing the
316 consistency between satellite and suborbital data when compared to a global 3-D CTM as a
317 common intercomparison platform (Zhang et al., 2010). It considerably increases the range of
318 suborbital measurements that can be used because collocation in space and time is not required.
319 Indirect validation can also be conducted formally by chemical data assimilation of the different
320 observational data streams into the CTM.

321 The standard benchmark for direct validation of solar backscatter satellite observations is
322 the worldwide Total Carbon Column Observing Network (TCCON) (Wunch et al., 2011).
323 TCCON consists of ground-based Fourier Transform Spectrometer (FTS) instruments staring at
324 the Sun and detecting methane absorption in the direct solar radiation spectrum. This measures
325 the same dry-air column mole fraction X_{CH_4} as the satellite but with much better signal-to-noise
326 and a well-defined light path. The TCCON retrieval of methane is calibrated to the World
327 Meteorological Organization (WMO) scale and has been validated by comparison to aircraft
328 profiles (Wunch et al., 2011). The single-observation precision and bias for X_{CH_4} are both about 4
329 ppb (Buchwitz et al., 2015).

330 Dils et al. (2014) and Buchwitz et al. (2015) present direct validation of the different
331 operational SCIAMACHY and GOSAT retrievals using TCCON data. Relative bias is
332 determined using pairs of TCCON sites. They find a single-observation precision of 30 ppb and
333 relative bias of 4-13 ppb for SCIAMACHY in 2003-2005, good enough for inverse applications,
334 but worsening after 2005 to 50-82 ppb (precision) and 15 ppb (relative bias). For GOSAT, they
335 report single-observation precisions of 12-13 ppb for the CO₂ proxy products and 15-16 ppb for
336 the full-physics products. Relative biases for GOSAT are 2-3 ppb for the CO₂ proxy products
337 and 3-8 ppb for the full-physics products. Thus the GOSAT data are of high quality for use in
338 inversions. The CO₂ proxy retrievals provide a much higher density of observations than the full-
339 physics retrievals, so that random errors can be effectively decreased and the precision improved
340 through temporal averaging.

341 TIR measurements are most sensitive to the middle/upper troposphere (Fig. 3) and
342 aircraft vertical profiles provide the best resource for direct validation. Wecht et al. (2012) and
343 Alvarado et al. (2015) evaluated successive versions of TES methane retrievals with data from
344 the HIPPO pole-to-pole aircraft campaigns over the Pacific (Wofsy, 2011). Alvarado et al.
345 (2015) report that the latest Version 6 of the TES product has a relatively large bias when
346 attempting to retrieve two pieces of information in the vertical but a bias of only 4.8 ppb when
347 retrieving just one piece of information. Crevoisier et al. (2011) found that IASI observations
348 are consistent with aircraft observations to within 5 ppb.

349 Use of satellite observations in inverse modeling studies cannot simply rely on past
350 validation to quantify the instrument error. This is because the instrument calibration may drift
351 with time, optics and detectors may degrade, and errors may vary depending on surface and
352 atmospheric conditions. It is essential that error characterization be done for the specific
353 temporal and spatial window of the inversion. Opportunities for direct validation may be sparse
354 but indirect validation with the CTM to be used for the inversion is particularly effective. Such
355 indirect validation can exploit all relevant suborbital data collected in the window to assess their
356 consistency with the satellite data. This has been standard practice in inversions of
357 SCIAMACHY and GOSAT data, and has resulted in correction factors applied to the data as a
358 function of latitude (Bergamaschi et al., 2009, 2013; Fraser et al., 2013; Alexe et al., 2015;



359 Turner et al., 2015), water vapor (Houweling et al., 2014; Wecht et al., 2014a), or air mass factor
360 (Cressot et al., 2014).

361

362 **3. Inferring methane emissions from satellite data**

363

364 **3.1 Overview of inverse methods**

365

366 We present here a brief overview of inverse methods as needed for understanding their
367 use to estimate methane emissions from satellite data. The general approach for inferring
368 methane emissions from observed atmospheric concentrations is to use a 3-D CTM describing
369 the sensitivity of concentrations to emissions. The CTM simulates atmospheric transport on the
370 basis of assimilated meteorological data for the observation period and a 2-D field of gridded
371 emissions. It computes concentrations as a function of emissions by solving the mass continuity
372 equation that describes the change in the 3-D concentration field resulting from emissions,
373 winds, turbulence, and chemical loss. In Eulerian CTMs, the solution to the continuity equation
374 is done on a fixed atmospheric grid. In Lagrangian CTMs, often called Lagrangian Particle
375 Dispersion Models (LPDMs), the solution is obtained by tracking a collection of air particles
376 moving with the flow. Eulerian models have the advantage of providing a complete, continuous,
377 and mass-conserving representation of the atmosphere. LPDMs have the advantage of being
378 directly integrable backward in time, so that the source footprint contributing to the
379 concentrations at a particular receptor point is economically computed. Eulerian models can also
380 be integrated backward in time to derive source footprints using the model adjoint (Henze et al.,
381 2007). LPDMs have been used extensively for inverse analyses of ground and aircraft methane
382 observations, where the limited number of receptor points makes the Lagrangian approach very
383 efficient (Miller et al., 2013; Ganesan et al., 2015; Henne et al., 2016). Satellite observations
384 involve a considerably larger number of receptor points, including different altitudes contributing
385 to the column measurement. For this reason, all published inversions of satellite methane data so
386 far have used Eulerian CTMs. A preliminary study by Benmergui et al. (2015) applies an LPDM
387 to inversion of GOSAT data.

388 The CTM provides the sensitivity of concentrations to emissions at previous times. By
389 combining this information with observed concentrations we can solve for the emissions needed
390 to explain the observations. Because of errors in measurements and in model transport, the best
391 that can be achieved is an error-weighted statistical fit of emissions to the observations. This
392 must account for prior knowledge of the distribution of emissions, generally from a bottom-up
393 inventory, in order to target the fit to the most relevant emission variables and in order to achieve
394 an optimal estimate of emissions consistent with all information at hand.

395 The standard method for achieving such a fit is Bayesian optimization. The emissions are
396 assembled into a state vector \mathbf{x} (dim n), and the observations are assembled into an observation
397 vector \mathbf{y} (dim m). Bayes' theorem gives

$$398 \quad P(\mathbf{x}|\mathbf{y}) = \frac{P(\mathbf{x})P(\mathbf{y}|\mathbf{x})}{P(\mathbf{y})} \quad (3)$$

399

400 where $P(\mathbf{x})$ and $P(\mathbf{y})$ are the probability density functions (PDFs) of \mathbf{x} and \mathbf{y} , $P(\mathbf{x}|\mathbf{y})$ is the
401 conditional PDF of \mathbf{x} given \mathbf{y} , and $P(\mathbf{y}|\mathbf{x})$ is the conditional PDF of \mathbf{y} given \mathbf{x} . We recognize here
402 $P(\mathbf{x})$ as the prior PDF of \mathbf{x} before the observations \mathbf{y} have been made, $P(\mathbf{y}|\mathbf{x})$ as the observation



403 PDF given the true value of \mathbf{x} (for which the observations were made), and $P(\mathbf{x}|\mathbf{y})$ as the
 404 posterior PDF of \mathbf{x} after the observations \mathbf{y} have been made. The optimal estimate of emissions is
 405 defined by the maximum of $P(\mathbf{x}|\mathbf{y})$, which we obtain by solving $\nabla_{\mathbf{x}}P(\mathbf{x}|\mathbf{y}) = \mathbf{0}$.

406 In the absence of better information, error PDFs are generally assumed to be Gaussian
 407 (Rodgers, 2000). We then have

$$408 \quad P(\mathbf{x}) = \frac{1}{(2\pi)^{n/2} |\mathbf{S}_A|^{1/2}} \exp\left[-\frac{1}{2}(\mathbf{x} - \mathbf{x}_A)^T \mathbf{S}_A^{-1}(\mathbf{x} - \mathbf{x}_A)\right] \quad (4)$$

$$409 \quad P(\mathbf{y}|\mathbf{x}) = \frac{1}{(2\pi)^{m/2} |\mathbf{S}_O|^{1/2}} \exp\left[-\frac{1}{2}(\mathbf{y} - \mathbf{F}(\mathbf{x}))^T \mathbf{S}_O^{-1}(\mathbf{y} - \mathbf{F}(\mathbf{x}))\right] \quad (5)$$

410 where \mathbf{x}_A is the prior estimate, \mathbf{S}_A is the associated prior error covariance matrix, \mathbf{F} is the CTM
 411 solving for $\mathbf{y} = \mathbf{F}(\mathbf{x})$ and is called the forward model for the inversion, and \mathbf{S}_O is the observational
 412 error covariance matrix including contributions from measurement and CTM errors. An
 413 important assumption here is that the observational error is random; any known systematic bias
 414 in the measurement or the CTM must be removed before the inversion is conducted. This
 415 requires careful validation (Sect. 2.2).

417 The optimization problem $\nabla_{\mathbf{x}}P(\mathbf{x}|\mathbf{y}) = \mathbf{0}$ is solved by minimizing the cost function $J(\mathbf{x})$:

$$418 \quad J(\mathbf{x}) = (\mathbf{x} - \mathbf{x}_A)^T \mathbf{S}_A^{-1}(\mathbf{x} - \mathbf{x}_A) + (\mathbf{y} - \mathbf{F}(\mathbf{x}))^T \mathbf{S}_O^{-1}(\mathbf{y} - \mathbf{F}(\mathbf{x})) \quad (6)$$

419 where the PDFs have been converted to their logarithms and the terms independent of \mathbf{x} have
 420 been discarded. In particular, $P(\mathbf{y})$ in Eq. (3) is discarded since it does not depend on \mathbf{x} . The
 421 minimum of J is found by differentiating Eq. (6):
 422

$$423 \quad \nabla_{\mathbf{x}}J(\mathbf{x}) = 2\mathbf{S}_A^{-1}(\mathbf{x} - \mathbf{x}_A) + 2\mathbf{K}^T \mathbf{S}_O^{-1}(\mathbf{F}(\mathbf{x}) - \mathbf{y}) = \mathbf{0} \quad (7)$$

424 where $\mathbf{K} = \nabla_{\mathbf{x}}\mathbf{F} = \partial\mathbf{y} / \partial\mathbf{x}$ is the Jacobian of \mathbf{F} and \mathbf{K}^T is its adjoint.
 425

426 **Analytical method.** Equation (7) can be solved analytically if the relationship between
 427 emissions and atmospheric concentrations is linear, such that $\mathbf{F}(\mathbf{x}) = \mathbf{K}\mathbf{x} + \mathbf{c}$ where \mathbf{c} is a
 428 constant. This is the case for methane if the tropospheric OH concentration field used in the
 429 CTM to compute methane loss is not affected by changes in methane. Although methane and OH
 430 levels are interdependent because methane is a major OH sink (Prather, 1996), the global
 431 methane loading relevant for computing OH concentrations is well known (Prather et al., 2012).
 432 It is therefore appropriate to treat OH concentrations as decoupled from methane in the
 433 inversion. Analytical solution of Eq. (7) for a linear model $\mathbf{y} = \mathbf{F}(\mathbf{x})$ (where the constant \mathbf{c} can be
 434 simply subtracted from the observations) yields an optimal estimate $\hat{\mathbf{x}}$ with Gaussian error
 435 characterized by an error covariance matrix $\hat{\mathbf{S}}$ (Rodgers, 2000):
 436

$$437 \quad \hat{\mathbf{x}} = \mathbf{x}_A + \mathbf{G}(\mathbf{y} - \mathbf{K}\mathbf{x}_A) \quad (8)$$

438



439
$$\hat{\mathbf{S}} = (\mathbf{K}^T \mathbf{S}_0^{-1} \mathbf{K} + \mathbf{S}_A^{-1})^{-1} \quad (9)$$

440

441 Here \mathbf{G} is the gain matrix given by

442
$$\mathbf{G} = \mathbf{S}_A \mathbf{K}^T (\mathbf{K} \mathbf{S}_A \mathbf{K}^T + \mathbf{S}_0)^{-1} \quad (10)$$

443

444 The degree to which the observations constrain the state vector of emissions is diagnosed by the
 445 averaging kernel matrix $\mathbf{A} = \partial \hat{\mathbf{x}} / \partial \mathbf{x} = \mathbf{G} \mathbf{K} = \mathbf{I}_n - \hat{\mathbf{S}} \mathbf{S}_A^{-1}$ expressing the sensitivity of the optimized
 446 estimate to the actual emissions \mathbf{x} . Here \mathbf{I}_n is the $n \times n$ identity matrix. The observations may
 447 adequately constrain some features of the emission field and not others. The number of
 448 independent pieces of information on the emission field provided by the observing system is
 449 given by the trace of \mathbf{A} and is called the degrees of freedom for signal (DOFS = $\text{tr}(\mathbf{A})$).

450 Analytical solution to the inverse problem provides full error characterization of the
 451 solution through $\hat{\mathbf{S}}$ and \mathbf{A} . This is a very attractive feature, particularly for an underconstrained
 452 problem where we need to understand what information the observations actually provide.
 453 However, it requires explicit construction of the Jacobian matrix. With an Eulerian CTM this
 454 requires n individual simulations, each providing a column j of the Jacobian $\partial y_i / \partial x_j$. With an
 455 LPDM (or the adjoint of an Eulerian CTM), this requires m individual simulations tracking the
 456 backward transport from a given observation location and providing a row i of the Jacobian
 457 $\partial y_i / \partial \mathbf{x}$. Either way is a computational challenge when using a very large number m of satellite
 458 observations to optimize a very large number n of emission elements with high resolution.

459 Equations (8)-(10) further require the multiplication and inversion of large matrices of
 460 dimensions m and n . This curse of dimensionality can be alleviated by ingesting the observations
 461 sequentially as uncorrelated data packets (thus effectively reducing m) (Rodgers, 2000) and by
 462 recognizing that individual state vector elements have only a limited zone of influence on the
 463 observations (thus effectively reducing n or taking advantage of sparse-matrix methods) (Bui-
 464 Thanh et al., 2012). When observations are ingested sequentially for successive time periods
 465 with each packet used to update emissions for the corresponding period we refer to the method as
 466 a Kalman filter.

467 There is danger in over-interpreting the posterior error covariance matrix $\hat{\mathbf{S}}$ when the
 468 number of observations is very large, as from a satellite data set, because of the implicit
 469 assumption that observational errors are truly random and are representatively sampled over the
 470 PDF. CTM errors are rarely unbiased and generally not representatively sampled. Thus $\hat{\mathbf{S}}$ tends
 471 to be an over-optimistic characterization of the error on the optimal estimate. An alternate
 472 approach for error characterization is to compute an ensemble of solutions with modified prior
 473 estimates, forward model, inverse methods, or error estimates (Heald et al., 2004; Henne et al.,
 474 2016).

475

476 **Adjoint method.** The limitation on the size of the emission state vector can be lifted by solving
 477 equation (7) numerically instead of analytically. This is done by applying iteratively the adjoint
 478 of the CTM, which is the model operator \mathbf{K}^T , to the error-weighted model-observation
 479 differences $\mathbf{S}_0^{-1}(\mathbf{F}(\mathbf{x}) - \mathbf{y})$. We discussed above how this backward transport provides the
 480 sensitivity of concentrations to emissions at prior times, i.e., the footprint of the concentrations.



481 Here we apply it to determine the footprint of the errors in emissions as diagnosed by the model-
 482 observation differences. For an Eulerian CTM the adjoint must be independently constructed
 483 (Henze et al., 2007), while for a LPDM it is simply obtained by transporting the air particles
 484 backward in time.

485 The iterative procedure in the adjoint method is as follows. Starting from the prior
 486 estimate \mathbf{x}_A as initial guess, we apply the adjoint operator \mathbf{K}^T to the error-weighted model-
 487 observation differences $\mathbf{S}_0^{-1}(\mathbf{F}(\mathbf{x}_A) - \mathbf{y})$ and in this manner determine the sensitivity of these
 488 differences to emissions earlier in time; this defines the cost function gradient $\nabla_{\mathbf{x}} J(\mathbf{x}_A)$ in
 489 equation (7). By applying $\nabla_{\mathbf{x}} J(\mathbf{x}_A)$ to \mathbf{x}_A with a steepest-descent algorithm we obtain a next
 490 guess \mathbf{x}_1 for the minimum of $J(\mathbf{x})$, compute the corresponding vector $\mathbf{K}^T \mathbf{S}_0^{-1}(\mathbf{F}(\mathbf{x}_1) - \mathbf{y})$, and add
 491 the error-weighted difference from the prior estimate $\mathbf{S}_A^{-1}(\mathbf{x}_1 - \mathbf{x}_A)$ to obtain the cost function
 492 gradient $\nabla_{\mathbf{x}} J(\mathbf{x}_1)$. By applying $\nabla_{\mathbf{x}} J(\mathbf{x}_1)$ to \mathbf{x}_1 with the steepest-descent algorithm we obtain a
 493 next guess \mathbf{x}_2 , and iterate in this manner to find the minimum of $J(\mathbf{x})$ (Henze et al. 2007). A
 494 major advantage of the adjoint method is that the Jacobian is never explicitly computed, and
 495 there are no multiplication/inversion operations involving large matrices. Thus there is no
 496 computational limitation on the dimension of \mathbf{x} . Another major advantage is that the error PDFs
 497 do not need to be Gaussian. A drawback is that error characterization is not included as part of
 498 the solution. Approximate methods are available at additional computational cost to estimate the
 499 posterior error covariance matrix $\hat{\mathbf{S}}$ and from there the averaging kernel matrix \mathbf{A} (Bousserez et
 500 al., 2015).
 501

502 **MCMC methods.** Markov Chain Monte Carlo (MCMC) methods are yet another approach to
 503 solve the Bayesian inverse problem. Here the posterior PDF $P(\mathbf{x}|\mathbf{y})$ is constructed by direct
 504 computation from equation (3) using stochastic sampling of the \mathbf{x} domain and with given forms
 505 for $P(\mathbf{x})$ and $P(\mathbf{y}|\mathbf{x})$. These forms may be Gaussian, as in Eqs. (4) and (5), but not necessarily so.
 506 Starting from the prior estimate \mathbf{x}_A , we compute $P(\mathbf{x}_A)$ and $P(\mathbf{y}|\mathbf{x}_A)$, and from there compute
 507 $P(\mathbf{x}_A|\mathbf{y})$ using Eq. (3). We then define a next element of the Markov chain as $\mathbf{x}_1 = \mathbf{x}_A + \Delta\mathbf{x}$ where
 508 $\Delta\mathbf{x}$ is a random increment, compute $P(\mathbf{x}_1|\mathbf{y})$, and so on. With a suitable algorithm to sample
 509 representatively the \mathbf{x} domain as successive elements of the Markov chain, the full structure of
 510 $P(\mathbf{x}|\mathbf{y})$ is eventually constructed. Miller et al. (2014) and Ganesan et al. (2015) used MCMC
 511 methods in regional inversions of suborbital methane data. A major advantage is that the prior
 512 and observation PDFs can be of any form. For example, the prior PDF can include a “fat tail” to
 513 allow for the possibility of a point source behaving as a “super-emitter” either continuously or
 514 sporadically (Zavala-Araiza et al., 2015). Another advantage is that the full posterior PDF of the
 515 solution is obtained (not just the optimal estimate). The main drawback is the computational cost
 516 of exploring the n -dimensional space defined by \mathbf{x} .

517 There are other ways of expressing the prior information than as $(\mathbf{x}_A, \mathbf{S}_A)$. In the
 518 hierarchical Bayesian approach (Ganesan et al., 2014), information on the prior is optimized as
 519 part of the inversion. In the geostatistical approach (Michalak et al., 2006), prior information is
 520 expressed in terms of emission patterns rather than magnitudes. The cost function in the
 521 geostatistical inversion is

$$522 \quad J(\mathbf{x}, \boldsymbol{\beta}) = (\mathbf{x} - \mathbf{P}\boldsymbol{\beta})^T \mathbf{S}^{-1}(\mathbf{x} - \mathbf{P}\boldsymbol{\beta}) + (\mathbf{y} - \mathbf{F}(\mathbf{x}))^T \mathbf{S}_0^{-1}(\mathbf{y} - \mathbf{F}(\mathbf{x})) \quad (11)$$



523

524 where the $n \times q$ matrix \mathbf{P} describes the q different state vector patterns, with each column of \mathbf{P}
525 describing a normalized pattern such as the distribution of livestock. The unknown vector $\boldsymbol{\beta}$ of
526 dimension q gives the mean scaling factor for each pattern. Thus $\mathbf{P}\boldsymbol{\beta}$ represents a prior model for
527 the mean, with $\boldsymbol{\beta}$ to be optimized as part of the inversion. The covariance matrix \mathbf{S} gives the prior
528 covariance of \mathbf{x} , rather than the error covariance.

529 Inverse methods for constraining emissions can be applied not only to current observing
530 systems but also to evaluate formally the capability of a proposed future instrument to improve
531 current knowledge. Given an observation plan and error specifications for the proposed
532 instrument, we can compute the expected observational error covariance matrix \mathbf{S}_o . Given the
533 prior information ($\mathbf{x}_A, \mathbf{S}_A$) informed by the current observing system (from an inversion without
534 the proposed instrument), we can quantify the information added by the proposed instrument by
535 computing $\hat{\mathbf{S}}$ from Eq. (9) or an adjoint-based approximation (Bousserez et al., 2015). From
536 there we obtain the averaging kernel matrix $\mathbf{A} = \mathbf{I}_n - \hat{\mathbf{S}}\mathbf{S}_A^{-1}$ and the DOFS, and compare to the
537 DOFS without the instrument to quantify the information to be gained. This assessment will tend
538 to be optimistic because of the assumption that errors are random, well characterized, and
539 representatively sampled, as discussed above. But at least it demonstrates the potential of the
540 proposed instrument. Applications are presented in Sect. 3.4.

541 The simple error analysis described above to assess the value of a future instrument is
542 sometimes loosely called an observing system simulation experiment (OSSE). However, the
543 OSSE terminology is generally reserved for a more rigorous test (and an actual ‘experiment’) of
544 the benefit of adding the proposed instrument to the current observing system, including realistic
545 accounting of CTM errors. A standard OSSE setup is illustrated in Fig. 6. The OSSE uses two
546 CTMs driven by different assimilated meteorological datasets for the same period. The first
547 model (CTM1) produces a synthetic 3-D field of atmospheric concentrations from an emission
548 inventory taken as the “true” emissions (A in Fig. 6). For purpose of the exercise, CTM1 is taken
549 to have no error and so describes the “true” 3-D field of atmospheric concentrations. This “true”
550 atmosphere is then sampled synthetically with the current observing system, adding instrument
551 noise as stochastic random error, so that the resulting synthetic data mimic the current observing
552 system. Inversion of these data returns emissions optimized by the current observing system (B
553 in Fig. 6) We then add the proposed instrument to the observing system, again adding instrument
554 noise as random error on the basis of the instrument specifications, and invert the data using the
555 previously optimized emissions (B) as prior estimate. The resulting optimized emissions (C in
556 Fig. 6) can be compared to the “true” emissions (A) and to the prior emissions (B) to quantify the
557 value of the proposed instrument and its advantage relative to the current observing system. The
558 use of two independent assimilated meteorological data sets is important for this exercise as it
559 allows a realistic accounting of the CTM error component. Such an OSSE setup is frequently
560 used to evaluate proposed meteorological instruments, and it has previously been applied to the
561 evaluation of a geostationary instrument for tropospheric ozone (Zoogman et al., 2014) but not
562 so far for methane.

563

564 3.2 Specific issues in applying inverse methods to satellite methane data

565

566 There are a number of issues requiring care in the application of inverse methods to
567 estimate methane emissions from observations of atmospheric methane, some of which are
568 specific to satellite observations.



569

570 **Selection of emission state vector.** A first issue relates to the resolution of the emission field
571 (state vector) to be optimized by the inversion. Methane originates from a large number of
572 scattered sources, with emission factors that are poorly known and highly variable for a given
573 source sector. It is therefore of interest to optimize emissions with fine spatial resolution, and for
574 some sources also with fine temporal resolution. The resolution of the emission state vector can
575 in principle be as fine as the grid resolution and time step of the CTM used as forward model.
576 However, the amount of information contained in the observations places limits on the extent to
577 which emissions can actually be resolved. Satellite data sets may be large but the data are noisy.
578 If the dimension of the emission state vector is too large relative to the information content of the
579 observations, then the Bayesian optimization problem is underconstrained and the solution may
580 be heavily weighted by the prior estimate. This is known as the smoothing error and the
581 associated error covariance matrix is $(\mathbf{I}_n - \mathbf{A})\mathbf{S}_A(\mathbf{I}_n - \mathbf{A})^T$ (Rodgers, 2000). Smoothing is not a
582 problem *per se* if the off-diagonal structure of \mathbf{S}_A is well-characterized, so that information can
583 propagate between state vector elements; but it generally is not. When \mathbf{S}_A is specified diagonal,
584 as is often the case, the ability to depart from the prior estimate and reduce the posterior error
585 will be artificially suppressed if the dimension of \mathbf{x} is too large (Wecht et al., 2014a).

586 Figure 7 illustrates the smoothing problem in an inversion of methane emissions over
587 North America using SCIAMACHY. The remedy is to reduce the dimension of the emission
588 state vector, by aggregating state vector elements and optimizing only the aggregate (Fig. 7).
589 This introduces however another type of error, known as aggregation error, because the
590 relationship between aggregated state vector elements is now imposed by the prior estimate
591 (Kaminski et al., 2001). As shown by Turner and Jacob (2015) and illustrated in Fig. 7, it is
592 possible to define an optimal dimension of the emission state vector by balancing the smoothing
593 and aggregation errors. For a multi-annual GOSAT data set this implies a spatial resolution of
594 the order of 100-1000 km in methane source regions. The state vector of emissions can be
595 reduced optimally by hierarchical clustering (Wecht et al., 2014a) or by using radial basis
596 functions with Gaussian PDFs (Turner and Jacob, 2015).

597

598 **Bottom-up inventory used as prior estimate.** Inverse analyses require high-quality gridded
599 bottom-up inventories to regularize the solution and guide the interpretation of results. All
600 inversions of methane satellite data so far have relied on the EDGAR bottom-up inventory for
601 anthropogenic emissions with $0.1^\circ \times 0.1^\circ$ spatial resolution (European Commission, 2011), which
602 is presently the only global bottom-up inventory available on a fine grid. EDGAR relies on IPCC
603 (2006) default tier 1 methods that are relatively crude and it provides only limited classification
604 of methane emissions by source sector. Alexe et al. (2015) and Turner et al. (2015) find that
605 uncertainties in source patterns in the EDGAR inventory preclude the attribution of inventory
606 corrections from their GOSAT inversions to specific source sectors. Many individual countries
607 produce national inventories using more accurate IPCC tier 2/3 methods with individual
608 reporting of large sources and detailed breakdown by source sectors, but these inventories are
609 generally available only as national totals and are thus not usable for inversions.

610 The need for improved, finely gridded bottom-up inventories for inverse analyses is well
611 recognized. Wang and Bentley (2002) disaggregated the Australian national inventory to guide
612 inversion of surface observations at Cape Grim, Tasmania. Zhao et al. (2009) disaggregated the
613 California Air Resources Board (CARB) statewide inventory to a $0.1^\circ \times 0.1^\circ$ grid. Hiller et al.
614 (2014) disaggregated the Swiss national inventory to a 500×500 m² grid. Maasackers et al.



615 (2016) developed a gridded $0.1^\circ \times 0.1^\circ$ version of the national US emission inventory produced by
616 EPA (Fig. 1) and shows major differences with EDGAR in terms of source patterns even though
617 the national totals are similar.

618

619 **Positivity of the solution.** The standard assumption of Gaussian error PDFs for the prior
620 estimate allows for the possibility of negative methane emissions that are generally unphysical.
621 Small negative values may be acceptable as noise, and can be removed by averaging with
622 neighboring positive values. The analytical solution to the Bayesian inverse problem requires
623 Gaussian error PDFs (Sect. 3.1), but numerical solutions do not. Adjoint-based inversions may
624 use lognormal (Wecht et al., 2014a) or semi-exponential (Bergamaschi et al., 2013) error
625 distributions to prevent negative solutions. Miller et al. (2014) present additional approaches for
626 imposing positivity of the solution, including (1) application of Karush-Kuhn-Tucker (KKT)
627 conditions, and (2) MCMC methods with sampling domain restriction. These approaches will
628 tend to bias the solution by enforcing zero values for a subset of the state vector (KKT
629 conditions) or by artificially inflating the PDF of the prior estimate in the vicinity of zero
630 (MCMC methods).

631

632 **Variability in the methane background.** Observations from the HIPPO pole-to-pole aircraft
633 campaigns over the Pacific in 2010-2011 indicate background concentrations of tropospheric
634 methane varying with latitude from 1750-1800 ppb in the southern hemisphere to 1850-1900 ppb
635 at high northern latitudes (Wofsy, 2011). The mid-latitudes background varies on synoptic scales
636 under the alternating influence of high-latitude and low-latitude air masses. This variability in
637 background is comparable to the magnitude of concentration enhancements in methane source
638 regions, so that accurate accounting of the global methane background and its variability is
639 essential for regional inversions. Local source inversions may be able to use instead regional
640 background information upwind of the source (Krings et al., 2013).

641

642 Observations at remote sites from the NOAA Earth System Research Laboratory (ESRL)
643 network (Dlugokencky et al., 2011; Andrews et al., 2014) accurately characterize the seasonal
644 latitude-dependent background, and one can then rely on the CTM used as forward model in the
645 inversion to resolve the synoptic variations in that background. Global inversions of satellite data
646 have exploited the NOAA ESRL network data in different ways. Bergamaschi et al. (2009,
647 2013), Fraser et al. (2013), and Alexe et al. (2015) included the data in their inversions together
648 with the satellite data. Cressot et al (2014) conducted separate inversions with NOAA/ESRL and
649 satellite data, and demonstrated consistency between the two. In limited-domain inversions such
650 as on the continental scale of North America, the background must be specified as a time- and
651 latitude-dependent boundary condition. This has been done by Miller et al. (2013) using the
652 NOAA/ESRL data as boundary conditions, in Wecht et al. (2014a) by optimizing the boundary
653 conditions as part of the inversion, and by Turner et al. (2015) by using results from a global
654 inversion as boundary conditions for the continental-scale inversion.

654

655 **Methane sink in the troposphere.** The main sink for methane is oxidation by the OH radical in
656 the troposphere, with a lifetime of 9 years constrained by global observations of
657 methylchloroform (MCF) (Prather et al., 2012). OH is produced photochemically and its
658 concentration is controlled by complex chemistry that is not well represented in models
659 (Voulgarakis et al., 2013). However, the loss of methane is sufficiently slow that variability in
660 OH concentrations affects methane concentrations only on seasonal, interannual, and



661 interhemispheric scales (Bousquet et al., 2006). It does not affect the regional-scale gradients
662 relevant to inverse analyses of satellite data. Global inverse analyses generally compute the
663 methane sink by using specified global 3-D monthly fields of OH concentrations from an
664 independent simulation of tropospheric oxidant chemistry and compatible with the MCF
665 constraint (Bergamaschi et al, 2013; Houweling et al., 2014). Cressot et al. (2014) optimized
666 methane and MCF emissions together in their inversion, thus allowing for adjustment of OH
667 concentrations within the uncertainty range allowed by MCF. Specifying OH concentrations is
668 not an issue for limited-domain inversions with spatial boundary conditions, because the
669 modeling domain is then ventilated on a time scale considerably shorter than the 9-year methane
670 lifetime. In that case, information on the methane sink is effectively incorporated in the boundary
671 conditions.

672

673 **Stratospheric methane.** Inversions of satellite methane data require a proper accounting of the
674 stratosphere. The stratosphere accounts for about 5% of the total methane column in the tropics
675 and 25% at high latitudes (Ostler et al., 2015). Methane enters the stratosphere in the tropics and
676 is transported to high latitudes on a time scale of about 5 years. Over that time it is
677 photochemically oxidized by OH, O(¹D), and Cl atoms, leading to a seasonal variation in the
678 column mean mole fraction X_{CH_4} out of phase with tropospheric methane (Saad et al., 2014).
679 Meridional transport in the stratosphere tends to be too fast in models, so that stratospheric
680 methane concentrations at high latitudes are overestimated (Patra et al., 2011). Not correcting for
681 this effect in inversions can lead to a 5% overestimate of the methane source at northern mid-
682 latitudes and a 40% overestimate in the Arctic (Ostler et al., 2015).

683

684 A number of observational data sets are available to evaluate the stratospheric methane
685 simulation in CTMs. These include balloons (Bergamaschi et al., 2013), TCCON stratospheric
686 retrievals (Saad et al., 2014), and satellite observations by solar occultation and in the limb
687 (deMaziere et al., 2008; von Clarmann et al., 2009; Noel et al., 2011; Minschwaner and Manney,
688 2014). Bergamaschi et al. (2013) presented a detailed evaluation of their CTM with balloon
689 observations as prelude to inversion of SCIAMACHY data, and this led them to limit their
690 inversion to the 50°S-50°N latitudinal range where model bias was small. Another approach is to
691 apply a latitudinal bias correction for the difference between the CTM and the satellite data
692 (Turner et al., 2015). Ostler et al. (2015) presented a method to correct for stratospheric methane
693 bias in CTMs by using constraints on the age of air in the stratosphere from vertical profiles of
694 sulfur hexafluoride (SF₆).

694

695 **Error characterization.** Estimation of prior and observational error covariances is crucial for
696 inverse modeling. Observational error is the sum of instrument and CTM errors. We discussed
697 in Sect. 2.2 the characterization of instrument error by validation with suborbital data. CTM error
698 variance can be estimated by intercomparison of different CTMs (Patra et al., 2011) and added to
699 the instrument error variance in quadrature. A better and more straightforward approach is to
700 estimate the total observational error variance by the residual error method (Heald et al., 2004),
701 which uses statistics of differences between the observations and the CTM concentrations
702 computed with prior emissions. Systematic difference (bias) is assumed to be caused by error in
703 emissions (to be corrected in the inversion), The remaining residual difference (averaging to
704 zero) defines the total observational error, including contributions from instrument and CTM
705 errors. This method has the merit of being consistent with the inversion premise that the
706 observational error is random. The CTM error variance can then be deduced by subtraction of the



707 instrument error variance. Application to SCIAMACHY and GOSAT shows that the instrument
708 error tends to be dominant (Wecht et al., 2014a; Turner et al., 2015). Error correlation populating
709 the off-diagonal terms of the observational error covariance matrix is typically specified as an e-
710 folding characteristic length scale (Heald et al., 2004).

711 Error in the prior bottom-up emission inventory is often crudely assumed to be a fixed
712 percentage (such as 50%), with no error correlation, for lack of better information. Although
713 some bottom-up emission inventories include error budgets produced by the bottom-up
714 methodology (EPA, 2016), these are generally not available in gridded inventories such as
715 EDGAR. An alternate approach is to intercompare independently generated bottom-up
716 inventories. This has been done for wetlands with the WETCHIMP intercomparison (Melton et
717 al., 2013) and for the $1^\circ \times 1^\circ$ gridded version of the US EPA anthropogenic methane inventory by
718 comparison to local inventories (Maasakkers et al., 2016). Error PDFs are usually assumed to be
719 normal or log-normal, but more skewed PDFs may better capture the occurrence of “super-
720 emitters” (Zavala-Areiza et al., 2015). The prior error covariance matrix is usually taken to be
721 diagonal, but some error correlation would in fact be expected for a given source sector. This is
722 accounted for in the geostatistical inversion approach (Eq. (11)) by assuming coherence in source
723 patterns. Scale dependence of the error must also be recognized, as errors in emissions for
724 individual grid squares increase with the grid resolution of the inventory (Maasakkers et al.,
725 2016).

726 Sources completely missing from the prior bottom-up inventory pose a particular
727 difficulty for inverse modeling, because inverse methods applied to an underconstrained problem
728 will tend to correct emissions where the prior estimate indicates them to be. Simply increasing
729 the error on the prior estimate is not a satisfactory approach because the inverse solution may
730 then misplace emissions. Before conducting the inversion it is important to compare the CTM
731 simulation using prior emissions to the observations, and diagnose whether any elevated values
732 in the observations that are absent in the simulation could represent missing sources.

733

734 **3.3 Applications to SCIAMACHY and GOSAT data**

735

736 Most inversions of SCIAMACHY and GOSAT satellite data for atmospheric methane
737 have been done on the global scale, estimating emissions at the resolution of the CTM used as
738 forward model (typically a few hundred km) by applying an adjoint method (Bergamaschi et al.,
739 2009, 2013; Spahni et al., 2011; Monteil et al., 2013; Cressot et al., 2014; Houweling et al. 2014;
740 Alexe et al., 2015). Fraser et al. (2013) estimated monthly methane fluxes over continental-scale
741 source regions by using an analytical method with a Kalman filter. Wecht et al. (2014a) and
742 Turner et al. (2015) used continental-scale inversions for North America to estimate emissions at
743 up to 50 km resolution in source regions through optimal selection of the state vector, with
744 Turner et al. (2015) applying an analytical inversion to characterize errors. Fraser et al. (2014)
745 and Pandey et al. (2015) optimized both methane and CO₂ fluxes using X_{CH_4}/X_{CO_2} ratios observed
746 from GOSAT, thus avoiding the need for independent specification of CO₂ concentrations in the
747 CO₂ proxy method for methane retrieval. Cressot et al. (2014) and Alexe et al. (2015) compared
748 results from inversions using different SCIAMACHY and GOSAT retrievals, and found overall
749 consistency in different regions of the world; however, Cressot et al. (2014) pointed out large
750 errors when using the degraded post-2005 SCIAMACHY data (see Sect. 2.2).

751 Inversions of methane fluxes using GOSAT data show consistency with observations
752 from NOAA ESRL surface sites, both in joint inversions (Bergamaschi et al., 2009, 2013; Fraser



753 et al., 2013; Alexe et al., 2015) and in independent evaluations (Turner et al., 2015). GOSAT
754 observations are sparse, with observation points separated by about 260 km, but still provide
755 considerably more information on methane emissions at the continental scale than the surface
756 network observations (Fraser et al., 2013; Alexe et al., 2015). This is particularly true in the
757 tropics, where methane emissions are large but surface observations are few (Bergamaschi et al.,
758 2013; Cressot et al., 2014; Houweling et al., 2014).

759 Inversions of SCIAMACHY and GOSAT data have revealed important biases in bottom-
760 up inventories of methane emissions. Monteil et al. (2013) and Spahni et al. (2011) find large
761 errors in wetland emission models. Bergamaschi et al. (2013) find that 2003-2010 growth in
762 Chinese emissions is less than estimated by EDGAR. Inversion results in the US consistently
763 show that EDGAR emissions in the South-Central US are low while emissions along the East
764 Coast are high (Wecht et al., 2014a; Alexe et al., 2015; Turner et al., 2015).

765 Ultimately, the application of satellite data to improve understanding of methane
766 emissions requires that the optimized estimates from the inversions be related to specific source
767 sectors and processes in the bottom-up inventories. SCIAMACHY observations over wetlands
768 have been used in this manner to improve bottom-up models of wetland emissions (Spahni et al.,
769 2011; Bloom et al., 2010, 2012). Application of satellite observations to improve anthropogenic
770 emission inventories has so far been stymied by poor representation of emission patterns in the
771 inventories. For example, the EDGAR underestimate in the South-Central US cannot be
772 confidently attributed to livestock or oil/gas sectors because EDGAR emission patterns for these
773 sectors are grossly incorrect (Maasackers et al., 2016).

774 Satellite data sets for correlative variables could help relate methane observations to
775 source sectors but this has received little attention so far. Bloom et al. (2012) combined methane
776 data from SCIAMACHY with water height data from the GRACE satellite instrument to
777 improve their bottom-up inventory of wetland methane emissions. Worden et al. (2012)
778 combined measurements of methane and CO from TES to quantify methane emissions from
779 Indonesian fires. TIR measurements of ammonia are available from the TES, IASI, and CrIS
780 satellite instruments (Shephard et al., 2011; Van Damme et al., 2014; Shephard and Cady-
781 Pereira, 2015) and provide a fingerprint of livestock emissions (Zhu et al., 2013), but have yet to
782 be exploited in combination with methane satellite data. Ethane would provide a marker for
783 oil/gas emissions but is observed from space only by solar occultation with sensitivity limited to
784 the upper troposphere (Abad et al., 2011). TROPOMI will provide data for both methane and CO
785 from common SWIR retrievals. Beyond constraining the combustion source of methane, the CO
786 observations could be valuable to decrease model transport errors in joint methane-CO
787 inversions (Wang et al., 2009).

788

789 **3.4 Potential of future satellite observations**

790

791 Future satellite instruments listed in Table 1 will have higher pixel resolution, spatial
792 density, and temporal frequency than SCIAMACHY or GOSAT. Several studies have examined
793 how these attributes will improve the capability of methane flux inversions. Wecht et al. (2014b)
794 conducted an inversion of methane emissions in California at $1/2^\circ \times 2/3^\circ$ resolution using
795 boundary layer observations from the May-June 2010 CalNex aircraft campaign and concurrent
796 observations from GOSAT. They then estimated the information that TROPOMI or the GEO-
797 CAPE geostationary mission would have provided over the 2-month period through analysis of
798 the corresponding observational error correlation matrices. Inversion of the CalNex aircraft data



799 provided 12 independent pieces of information (DOFS) on the spatial distribution of emissions in
800 California as compared to 1.3 for GOSAT, 11 for TROPOMI, and 26 for GEO-CAPE.
801 TROPOMI could thus constrain emissions with a skill comparable to a dedicated statewide
802 aircraft campaign, and a geostationary mission with hourly observations would provide much
803 more. The study likely underestimated the capability of TROPOMI and GEO-CAPE to resolve
804 hotspots because of the coarse $1/2^\circ \times 2/3^\circ$ resolution of the forward model. We return to this
805 point in Sect. 4.

806 Bousserez et al. (2016) explored the potential of geostationary observations to constrain
807 methane emissions on the continental scale of North America over weekly and monthly time
808 scales. Again they used a CTM with $1/2^\circ \times 2/3^\circ$ spatial resolution as forward model and averaged
809 the $4 \times 4 \text{ km}^2$ geostationary observation pixels over that coarser grid with corresponding error
810 reduction. They considered three different configurations of geostationary instruments observing
811 hourly in the SWIR, TIR, and SWIR+TIR (multispectral retrieval). They found that SWIR
812 geostationary observations would effectively constrain methane emissions over the $1/2^\circ \times 2/3^\circ$
813 grid on a monthly time scale, while a combined SWIR+TIR instrument could deliver that
814 information on a weekly time scale.

815 Bovensmann et al. (2010) examined the potential of CarbonSat to detect methane point
816 sources by inversion of the Gaussian dispersion plume, and Rayner et al. (2014) did the same for
817 geoCARB. We review their results in the next Section.

818 4. Observing requirements for regional and point sources

819 Here we present a simple analysis of the potential of future satellite instruments for
820 observing regional and point sources from space. Observing requirements are somewhat
821 different for climate policy and for point source monitoring purposes. From a climate policy
822 standpoint, the goal is to quantify annual mean emissions with emphasis on the regional scale
823 and source attribution. This plays to the strength of satellites, as repeated observations of the
824 same scene measure the temporal average with improved precision, and also smooth out the
825 temporal variability that can bias estimates from short-term field campaign data. From a point
826 source monitoring standpoint, on the other hand, we may be most interested in detecting large
827 leaks or venting from facilities emitting far more than would be expected on the basis of normal
828 operations (the so-called “super-emitters”). Here the advantage of satellite data is spatial
829 coverage, but a requirement is to have a localized and detectable signal on short time scales, with
830 detection and localization being more important than precise quantification.

831 For conceptual purposes we define detection/quantification as the ability to observe the
832 methane enhancement ΔX [ppb] from a source relative to the surrounding background. Single-
833 scene instrument precisions σ [ppb] are taken from Table 1, and we make the optimistic
834 assumption that precision improves as the square root of the number of observations following
835 the central limit theorem (Kulawik et al., 2016). We define detectability as a precision of $\Delta X/2$
836 and quantification as a precision of $\Delta X/5$. Only a fraction F of pixels is successfully retrieved
837 because of clouds, unsuccessful spectral fits, or other factors. The time required for
838 detection/quantification of the source is then
839

$$840 \quad t = t_R \max \left[1, \frac{1}{FN} \max \left[1, \left(\frac{q\sigma}{\Delta X} \right)^2 \right] \right] \quad (12)$$



841

842 where N is the number of observations of the source for a single satellite pass, t_R is the time
 843 interval between passes, and q takes on values of 2 for detection and 5 for quantification.

844 We first examine the capability of satellite instruments to quantify emissions from a large
 845 source region by taking as example the Barnett Shale in Northeast Texas, a $300 \times 300 \text{ km}^2$ region
 846 with about 30,000 active wells as well as livestock operations and the Dallas/Fort Worth
 847 metropolitan area. An intensive field campaign was conducted in the region in September-
 848 October 2013 to characterize individual sources (Harriss et al., 2015). Synthesis of the data by
 849 Lyon et al. (2015) gives a total emission for the region of 72 tons h^{-1} . Take the Barnett Shale
 850 region as a square of side $W = 300 \text{ km}$ ventilated by a uniform wind of speed U . The mean
 851 enhancement ΔX relative to the upwind background is obtained by mass balance:
 852

$$853 \quad \Delta X = \frac{M_a}{M_{CH_4}} \frac{Qg}{UWp} \quad (13)$$

854

855 where $M_a = 0.029 \text{ kg mol}^{-1}$ and $M_{CH_4} = 0.016 \text{ kg mol}^{-1}$ are the molecular weights of dry air and
 856 methane, p is the dry atmospheric surface pressure, and $g = 9.8 \text{ m s}^{-2}$ is the acceleration of
 857 gravity. Taking $U = 5 \text{ km h}^{-1}$ and $p = 1000 \text{ hPa}$, and with $Q = 72 \text{ tons CH}_4 \text{ h}^{-1}$, we obtain $\Delta X =$
 858 8.5 ppb or 0.47% .

859 Table 2 summarizes the capabilities of the solar backscatter instruments in Table 1 to
 860 quantify such a source. GOSAT views 2-3 pixels for a $300 \times 300 \text{ km}^2$ region on a given orbit in its
 861 routine survey mode and has a return time of 3 days. The single-retrieval precision of GOSAT is
 862 0.7% or 13 ppb . 17% of GOSAT land pixels are retrieved successfully on average in the Parker
 863 et al. (2011) CO_2 proxy retrieval ($F = 0.17$). Replacement into Eq. (12) implies that it takes about
 864 1 year for GOSAT to effectively quantify emissions from the Barnett Shale. This explains why
 865 inverse analyses of GOSAT data retain substantial information from the prior as diagnosed by
 866 the averaging kernel matrix (Turner et al., 2015). A similar averaging time requirement applies
 867 to SCIAMACHY (2003-2005), which has denser observations but coarser precision and a
 868 smaller fraction of successful retrievals ($F = 0.09$). GOSAT-2 with an expected single-retrieval
 869 precision of 0.4% would reduce this time to about 4 months. TROPOMI will have full daily
 870 coverage of the Barnett Shale region with about 1,000 observing pixels, thus quantifying the
 871 regional emissions in a single day of observation.

872 Consider now the problem of detecting individual point sources through observations of
 873 the corresponding source pixels. We estimate for the different solar back-scatter instruments of
 874 Table 1 the detection threshold at the scale of a satellite pixel, and for a single observation pass,
 875 assuming low emissions in neighboring pixels (to characterize a local background) and clear
 876 skies (for favorable retrieval conditions). The enhancement ΔX in the source pixel is given by
 877 equation (13) but with W now representing the pixel size and with $N = 1$ and $F = 1$ in equation
 878 (12). By combining equations (12) and (13) we derive the minimum source Q_{\min} for single-pass
 879 detection as
 880

$$881 \quad Q_{\min} = \frac{M_{CH_4}}{M_a} \frac{UWpq\sigma}{g} \quad (14)$$

882



883 Table 2 gives the detection thresholds for the different satellite instruments with $U = 5$
884 km h^{-1} . These values can be compared to detailed point source information available for the US.
885 Figure 8 shows the high end of the distributions of annual emissions for (1) the gridded
886 $0.1^\circ \times 0.1^\circ$ EPA inventory of Maasackers et al. (2016), and (2) the 6887 individual point sources
887 reporting methane emissions to the EPA Greenhouse Gas Reporting Program (GHGRP).
888 Reporting to the GHGRP is required for all sources in excess of 25 Gg CO_2 equivalent a^{-1}
889 (corresponding to $0.1 \text{ tons CH}_4 \text{ h}^{-1}$ for a pure methane source). The GHGRP data include
890 combustion sources with very low methane emissions, hence Figure 8 only shows the top 15th
891 percentile of point sources (accounting for 85% of total GHGRP methane emissions). The largest
892 point sources in the GHGRP data with emissions in excess of 1 ton h^{-1} are underground coal
893 mines and landfills; individual point sources from oil/gas systems (compressor stations,
894 processing plants) are smaller. Emissions from natural gas production (including wells and
895 gathering stations) are reported to the GHGRP as basin totals instead of as point sources and are
896 thus not included in the point source distribution of Fig. 8 (but are included in the gridded
897 emissions). Individual “super-emitters” in oil/gas fields can emit in excess of 1 ton h^{-1} but likely
898 on an intermittent basis (Zavala-Areiza et al., 2015; Lyon et al., 2015).

899 Pixel resolution of the satellite instrument can be a limiting factor for detecting individual
900 point sources because these are often clustered on a 1-10 km scale (as in an oil/gas field) and/or
901 overlap with large area sources (gas distribution, livestock) (Lyon et al., 2015). For a satellite
902 instrument with pixel resolution $\sim 10 \text{ km}$, the frequency distribution of gridded $0.1^\circ \times 0.1^\circ$
903 ($\approx 10 \times 10 \text{ km}^2$) emissions in Fig. 8 is more relevant than that of GHGRP point sources.

904 Comparison of the detection thresholds in Table 2 to the emission distributions in Fig. 8
905 offers insight into the capabilities of the different instruments for resolving point sources. With a
906 detection limit of 4 tons h^{-1} (for a wind of 5 km h^{-1}), TROPOMI can detect in a single pass the 20
907 highest $0.1^\circ \times 0.1^\circ$ pixels in the gridded EPA inventory, contributing 5% of national emissions. It
908 would not detect a typical transient “super-emitter” of 1.0 tons h^{-1} in an oil/gas field in a single
909 overpass. Because of its full daily coverage, TROPOMI can be far more effective at detecting
910 sustained point sources and quantifying their annual emissions. For 365 successive passes (once
911 a day) and a successful retrieval rate of 17%, TROPOMI should be able to isolate individual
912 pixel sources of 0.5 tons h^{-1} , representing the top 1% of $0.1^\circ \times 0.1^\circ$ gridsquares in the EPA
913 inventory and amounting to 30% of total US emissions. GOSAT-2 has a similar single-pass
914 sensitivity to point sources as TROPOMI when observing in target mode but has much sparser
915 coverage.

916 GHGSat and CarbonSat are designed for observation of point sources. If it meets its
917 specifications of Table 1, GHGSat will have a single-pass detection threshold of 0.24 tons h^{-1}
918 (for a wind of 5 km h^{-1}). This will detect 700 of the GHGRP point sources in Fig. 8,
919 corresponding to 80% of the national total in the GHGRP point source inventory. A single
920 GHGSat instrument will have a return time of 2 weeks, limiting its ability to detect transient
921 “super-emitters”, but long-term plans are for a fleet of instruments on microsatellites.

922 Bovensmann et al. (2010) give a CarbonSat detection threshold of 0.24 tons h^{-1} for $U = 5$
923 km h^{-1} , based on inversion of data from a transported Gaussian plume. We find a threshold of 0.8
924 tons h^{-1} for single-pixel detection. Mapping of the methane plume in downwind pixels offers
925 additional opportunity for detecting/quantifying a point source as long as there is no overlap with
926 other sources and some model of plume transport is applied. Bovensmann et al. (2010) did not
927 include transport error in their analysis which may lead to overoptimistic results. With $2 \times 2 \text{ km}^2$
928 pixel resolution, CarbonSat would be limited in its ability to resolve the structure of individual



929 methane plumes, as airborne mapping shows plumes to be smaller in scale even for large point
930 sources (Krings et al., 2013; Thorpe et al., 2016; Frankenberg et al., 2016). The $0.05 \times 0.05 \text{ km}^2$
931 resolution of GHGSat, with imaging over a $12 \times 12 \text{ km}^2$ grid, has better potential for resolving
932 the plume structure. A complication in remote sensing of plumes with sub-km pixels is that one
933 may not assume that the incident and reflected solar rays (Fig. 2) sample the same boundary
934 layer methane column. The air mass factor calculation must trace the propagation of the incident
935 and reflected solar rays through the plume, taking into account the solar azimuth and zenith
936 angles as well as the altitude of the plume.

937 Several approaches have been used to exploit downwind plume information for inferring
938 point source emissions, including (1) inverse modeling with source strength and dispersion
939 parameters as state variables (Krings et al., 2011, 2013), (2) integrating the flux over the plume
940 cross-section normal to wind direction (Conley et al., 2016), and (3) summing the above-
941 background mass in all plume pixels and relating this integrated mass enhancement to emission
942 by using a relationship from known sources or a plume dispersion model (Frankenberg et al.,
943 2016). Choice of the best approach may depend on the level of meteorological information
944 available and the ability of the instrument to map the observed plume structure, which in turn
945 depends on the pixel size, the measurement noise, the ability to define the local background, and
946 the complexity of the flow including the effect of wind shear (Rayner et al., 2014).

947 Geostationary observations can in principle achieve high precision together with fine
948 pixel resolution because the viewing geometry allows much longer observation times. But there
949 is competing demand for spatial coverage. GEO-CAPE and geoCARB in their proposed
950 implementations (Table 1) expect to achieve 1% precision for $\sim 4 \times 4 \text{ km}^2$ pixels, limited by their
951 stated mission objectives to observe continental-scale domains every hour or few hours. With
952 this implementation and the above assumptions, a regional source such as the Barnett Shale is
953 strongly constrained on an hourly basis while a point source of 1.0 ton h^{-1} would require a week
954 of observation (Table 2). GeoFITS expects to achieve $< 0.2\%$ precision, greatly increasing the
955 capability to observe transient point sources. Point sources could be detected on a sub-daily time
956 scale from geostationary orbit by adopting longer viewing times per pixel and/or using finer
957 pixels. This could be achieved by limiting the domain of observation or by using “special
958 observations” where the instrument is maneuvered to stare at specific points of interest. For
959 example, detection of an anomaly in emissions, either from the satellite or from suborbital
960 observations, could motivate targeted observation by the satellite to localize and quantify the
961 anomaly. A schedule of alternate days for continental-scale mapping and for special observations
962 could be particularly effective in enabling a geostationary mission to effectively quantify
963 emissions at the national and regional scales while also providing fast detection and
964 quantification of point sources.

965 Airborne remote sensing offers another way to observe methane emissions from point
966 sources, using the same techniques as satellite remote sensing but with much higher spatial
967 resolution. MAMAP (Krings et al., 2011) retrieves methane in the SWIR at $1.6 \mu\text{m}$, similar to
968 SCIAMACHY, but currently lacks imaging capabilities. Imaging spectrometers initially
969 designed for surface remote sensing have been shown to detect methane plumes with spatial
970 resolution as fine as 1 m either in the SWIR using the strong $2.3 \mu\text{m}$ band (Roberts et al., 2010;
971 Thorpe et al., 2016) or in the TIR (Tratt et al., 2014; Hulley et al., 2016). These imaging
972 spectrometers such as AVIRIS-NG (SWIR) and MAKO or HyTES (TIR) have much coarser
973 spectral resolution than MAMAP or current satellite instruments (e.g., 5 nm for AVIRIS-NG).
974 However, at this fine spatial resolution, concentration enhancements over point sources are much



975 higher and can be discerned down to a detection threshold only 2 kg h^{-1} (Thorpe et al., 2016). A
976 major advantage is that the fine structure of the plume shape can be observed, allowing for
977 localized source attribution (Thompson et al., 2015; Thorpe et al, 2016).

978

979 **5. Conclusions and recommendations**

980

981 We have reviewed the capabilities for observing atmospheric methane from space and
982 their utility for improving knowledge of methane emissions through inverse analyses.
983 Observations by solar backscatter in the shortwave infrared (SWIR) are of most interest for
984 quantifying emissions because they are sensitive to the full atmospheric column down to the
985 surface. Current observations from the GOSAT satellite are of high quality but sparse. Through
986 inverse analyses and annual averaging they can quantify emissions in source regions on a 100-
987 1000 km scale. The TROPOMI instrument to be launched in late 2016 will be able to map
988 emissions daily on that scale and will also have the capability to detect and quantify large point
989 sources. As such it will significantly enhance the value of satellite measurements to serve the
990 needs of climate policy. The GHGSat instrument launched in 2016 with $50 \times 50 \text{ m}^2$ pixel
991 resolution over $12 \times 12 \text{ km}^2$ viewing domains will effectively detect methane point sources if it
992 meets its specification of 1-5% precision.

993 The ultimate goal of top-down inverse analyses of atmospheric observations is to guide
994 the improvement of bottom-up emission inventories. Bottom-up inventories relate emissions to
995 the underlying processes, and as such are the fundamental tools for climate policy and for
996 making future projections. There is the opportunity for considerable synergy between top-down
997 and bottom-up approaches by using high-quality bottom-up inventories as prior estimates in
998 inversions, and then using inversion results to improve the inventories. Exploiting this synergy
999 requires the construction of finely gridded, sector-resolved bottom-up inventories including
1000 scale-dependent error statistics.

1001 Geostationary observations (still at the proposal stage) hold considerable potential for
1002 monitoring methane emissions from space. The geostationary orbit allows sustained staring at
1003 individual pixels, providing a unique opportunity to infer emissions with both high spatial and
1004 temporal resolution on national scales. Current geostationary mission concepts (GEO-CAPE,
1005 geoCARB, GeoFTS) emphasize hourly mapping of emissions at the continental scale. This limits
1006 their pixel resolution and their precision. It is not clear that high-frequency continental-scale
1007 mapping from geostationary orbit is of much value if sufficient information is already available
1008 from a LEO instrument such as TROPOMI. It may be more effective for a geostationary mission
1009 to focus on selective observation of point sources and source regions, enabling finer pixel
1010 resolution and longer viewing times to resolve emissions at local scale including transient
1011 sources.

1012 More work needs to be done in exploiting correlative observations to increase the value
1013 of methane satellite data. Observations of ammonia from space are becoming mature and provide
1014 a marker of livestock emissions. Joint observations of methane and CO as from TROPOMI may
1015 help to reduce model transport error in inversions through methane-CO error correlations.
1016 Satellite mapping of surface properties can provide important correlative information, as already
1017 demonstrated for wetlands. Satellite data for soil moisture, gas flaring, and imagery of point
1018 sources could be integrated with available methane data to more effectively constrain methane
1019 emissions.



1020 Suborbital observations of methane from aircraft and from the ground are essential
1021 partners to satellite observation. Suborbital observations have unique capability for correlative
1022 measurements such as methane isotopes and ethane that can provide additional constraints on
1023 inversions. Methane anomalies detected from space need to be confirmed by field observations,
1024 which can pinpoint sources with far greater accuracy (down to the device scale) than is
1025 achievable from space. Suborbital platforms are also essential for continual validation of the
1026 satellite data. The prospect of improving satellite observations in the near future calls for the
1027 construction of a comprehensive atmospheric methane observing system to monitor emissions
1028 from global to local scales through coordination with improved suborbital observations, bottom-
1029 up inventories, and atmospheric transport models.

1030

1031 **Acknowledgments.** This work was funded by the NASA Carbon Monitoring System, by the
1032 NASA GEO-CAPE Atmospheric Sciences Working Group, by the ExxonMobil Upstream
1033 Research Company, and by the US DOE Advanced Research Projects Agency – Energy. KV
1034 acknowledges funding from the Smithsonian Astrophysical Observatory.

1035

1036 **References**

1037

- 1038 Abad, G.G., et al., Ethane, ethyne and carbon monoxide concentrations in the upper troposphere and lower
1039 stratosphere from ACE and GEOS-Chem: a comparison study, *Atmos. Chem. Phys.*, 11, 9927–9941, 2011.
- 1040 Alexe, M., P. Bergamaschi, A. Segers, R. Detmers, A. Butz, O. Hasekamp, S. Guerlet, R. Parker, H. Boesch, C.
1041 Frankenberg, R. A. Scheepmaker, E. Dlugokencky, C. Sweeney, S. C. Wofsy, and E. A. Kort, Inverse
1042 modelling of CH₄ emissions for 2010–2011 using different satellite retrieval products from GOSAT and
1043 SCIAMACHY, *Atmos. Chem. Phys.*, 15, 113–133, 2015.
- 1044 Anderson, G., S. Clough, F. Kneizys, J. Chetwynd, and E. Shettle, AFGL atmospheric constituent profiles (0–120
1045 km), Tech. Rep. AFGL-TR-86-0110, Air Force Geophys. Lab., Hanscom Air Force Base, Bedford, Mass.,
1046 1986.
- 1047 Andrews, A. E., Kofler, J. D., Trudeau, M. E., Williams, J. C., Neff, D. H., Masarie, K. A., Chao, D. Y., Kitzis, D.
1048 R., Novelli, P. C., Zhao, C. L., Dlugokencky, E. J., Lang, P. M., Crotwell, M.J., Fischer, M. L., Parker, M. J.,
1049 Lee, J. T., Baumann, D. D., Desai, A. R., Stanier, C. O., De Wekker, S. F. J., Wolfe, D. E., Munger, J. W., and
1050 Tans, P. P.: CO₂, CO, and CH₄ measurements from tall towers in the NOAA Earth System Research
1051 Laboratory's Global Greenhouse Gas Reference Network: instrumentation, uncertainty analysis, and
1052 recommendations for future high-accuracy greenhouse gas monitoring efforts, *Atmos. Meas. Tech.*, 7, 647–
1053 687, 2014.
- 1054 Barnet, C., et al., CrIS Trace Gas Data Users Workshop, 18 Sept 2014.
- 1055 Benmergui, J., et al., Integrating diverse observations of North American CH₄ into flux inversions in
1056 CarbonTrackerLagrange-CH₄, presented at the Fall 2015 meeting of the American Geophysical Union, 2015.
- 1057 Bergamaschi, P., Krol, M., Dentener, F., Vermeulen, A., Meinhardt, F., Graul, R., Ramonet, M., Peters, W. and
1058 Dlugokencky, E.: Inverse modelling of national and European CH₄ emissions using the atmospheric zoom
1059 model TM5, *Atmos. Chem. Phys.*, 5, 2431–2460, 2005.
- 1060 Bergamaschi, P., C. Frankenberg, J. F. Meirink, M. Krol, M. G. Villani, S. Houweling, F. Dentener, E. J.
1061 Dlugokencky, J. B. Miller, L. V. Gatti, A. Engel, and I. Levin, Inverse modeling of global and regional CH₄
1062 emissions using SCIAMACHY satellite retrievals, *J. Geophys. Res.*, 114, doi:10.1029/2009JD012287, 2009.
- 1063 Bergamaschi, P., S. Houweling, A. Segers, M. Krol, C. Frankenberg, R. A. Scheepmaker, E. Dlugokencky, S. C.
1064 Wofsy, E. A. Kort, C. Sweeney, T. Schuck, C. Brenninkmeijer, H. Chen, V. Beck, and C. Gerbig, Atmospheric
1065 CH₄ in the first decade of the 21st century: Inverse modeling analysis using SCIAMACHY satellite retrievals
1066 and NOAA surface measurements, *J. Geophys. Res. Atmos.*, 118, 7350–7369, 2013.
- 1067 Bloom, A.A., P.I. Palmer, A. Fraser, and D.S. Reay, Seasonal variability of tropical wetland CH₄ emissions: the role
1068 of the methanogen-available carbon pool, *Biogeosciences*, 9, 2821–2830, 2012.
- 1069 Bousquet, P., et al., Contribution of anthropogenic and natural sources to atmospheric methane variability, *Nature*,
1070 443, 439–443, 2006.



- 1071 Bousquet, P., B. Ringeval, I. Pison, E. J. Dlugokencky, E.-G. Brunke, C. Carouge, F. Chevallier, A. Fortems-
1072 Cheiney, C. Frankenberg, D. A. Hauglustaine, P. B. Krummel, R. L. Langenfelds, M. Ramonet, M. Schmidt, L.
1073 P. Steele, S. Szopa, C. Yver, N. Viovy and P. Ciais, Source attribution of the changes in atmospheric methane
1074 for 2006-2008, *Atmos. Chem. Phys.*, 11, 3689–3700, 2011.
- 1075 Bousserrez, N., et al., Improved analysis-error covariance matrix for high-dimensional variational inversions:
1076 application to source estimation using a 3D atmospheric transport model, *QJRMS*, DOI:10.1002/qj.2495,
1077 2015.
- 1078 Bousserrez, N., D.K. Henze, B. Rooney, A. Perkins, K.J. Wecht, A.J. Turner, V. Natraj, and J.R. Worden,
1079 Constraints on methane emissions in North America from future geostationary remote sensing
1080 measurements, *Atmos. Chem. Phys. Discuss.*, 15, 19017–19044, 2016.
- 1081 Bovensmann, H., M. Buchwitz, J.P. Burrows, M. Reuter, T. Krings, K. Gerilowski, O. Schneising, J. Heymann, A.
1082 Tretner, and J. Erzinger, A remote sensing technique for global monitoring of power plant CO₂ emissions
1083 from space and related applications, *Atmos. Meas. Tech.*, 3, 781–811, 2010.
- 1084 Brakeboer, B.N.A., Development of the structural and thermal control subsystems for an Earth observation
1085 microsatellite and its payload, M.S. Thesis, University of Toronto, 2015.
- 1086 Brandt, A.R., et al., Methane leaks from North American gas systems, *Science*, 343, 733-735, 2014.
- 1087 Brasseur, G.P., and D.J. Jacob, *Modeling of Atmospheric Chemistry*, Cambridge University Press, New York, 2016.
- 1088 Bruhwiler, L., E. Dlugokencky, K. Masarie, M. Ishizawa, A. Andrews, J. Miller, C. Sweeney, P. Tans, and D.
1089 Worthy, CarbonTracker-CH₄: an assimilation system for estimating emissions of atmospheric methane,
1090 *Atmos. Chem. Phys.*, 14, 8269–8293, 2014.
- 1091 Buchwitz, M., M. Reuter, H. Bovensmann, D. Pillai, J. Heymann, O. Schneising, V. Rozanov, T. Krings, J. P.
1092 Burrows, H. Boesch, C. Gerbig, Y. Meijer, and A. Löscher, Carbon Monitoring Satellite (CarbonSat):
1093 assessment of atmospheric CO₂ and 4 retrieval errors by error parameterization, *Atmos. Meas. Tech.*, 6, 3477–
1094 3500, 2013.
- 1095 Bui-Thanh, T., C. Burstedde, O. Ghattas, J. Martin, G. Stadler, and L.C. Wilcox (2012), Extreme-scale UQ for
1096 Bayesian inverse problems governed by PDEs, in *IEEE International Conference for High Performance*
1097 *Computing, Networking, Storage and Analysis*, Salt Lake City, Utah, Nov 2012.
- 1098 Buchwitz, M., et al., The Greenhouse Gas Climate Change Initiative (GHG-CCI): Comparison and quality
1099 assessment of near-surface-sensitive satellite-derived CO₂ and CH₄ global data sets, *Remote Sensing*
1100 *Environ.*, 162, 344-362, 2015.
- 1101 Butz, A., O.P. Hasekamp, C. Frankenberg, and I. Aben, Retrievals of atmospheric CO₂ from simulated space-borne
1102 measurements of backscattered near-infrared sunlight: accounting for aerosol effects, *Appl. Opt.*, 48, 3322-
1103 3336, 2010.
- 1104 Butz, A., et al., Toward accurate CO₂ and CH₄ observations from GOSAT, *Geophys. Res. Lett.*, 38, L14812, 2011.
- 1105 Butz, A., Galli, A., Hasekamp, O., Landgraf, J., Tol, P., and Aben, I.: TROPOMI aboard Precursor Sentinel-5
1106 Precursor: Prospective performance of CH₄ retrievals for aerosol and cirrus loaded atmospheres, *Remote Sens.*
1107 *Environ.*, 120, 267–276, 2012.
- 1108 Caulton, D.R., et al., Toward a better understanding and quantification of methane emissions from shale gas
1109 development, *PNAS*, 111, doi: 10.1073/pnas.1316546111, 2014.
- 1110 Clerbaux, C., J. Hadji-Lazaro, S. Turquety, G. Megie, and P.-F. Coheur, Trace gas measurements from infrared
1111 satellite for chemistry and climate applications, *Atmos. Chem. Phys.*, 3, 1495–1508, 2003.
- 1112 Conley, S., G. Franco, I. Faloona, D.R. Blake, J. Peischl, and T.B. Ryerson, Methane emissions from the 2015 Aliso
1113 Canyon blowout in Los Angeles, CA, *Science*, 351, 1317-1321, 2016.
- 1114 Cressot, C., Chevallier, F., Bousquet, P., Crevoisier, C., Dlugokencky, E. J., Fortems-Cheiney, A., Frankenberg, C.,
1115 Parker, R., Pison, I., Scheepmaker, R. A., Montzka, S. A., Krummel, P. B., Steele, L. P., and
1116 Langenfelds, R. L.: On the consistency between global and regional methane emissions inferred from
1117 SCIAMACHY, TANSO-FTS, IASI and surface measurements, *Atmos. Chem. Phys.*, 14, 577-592,
1118 doi:10.5194/acp-14-577-2014, 2014.
- 1119 Crevoisier, C., et al., The 2007–2011 evolution of tropical methane in the mid-troposphere as seen from space by
1120 MetOp-A/IASI, *Atmos. Chem. Phys.*, 13, 4279–4289, 2013.
- 1121 De Maziere, M., et al., Validation of ACE-FTS v2.2 methane profiles from the upper troposphere to the lower
1122 mesosphere, *Atmos. Chem. Phys.*, 8, 2421–2435, 2008
- 1123 Dils, B., et al., The Greenhouse Gas Climate Change Initiative (GHG-CCI): comparative validation of GHG-CCI
1124 SCIAMACHY/ENVISAT and TANSO-FTS/GOSAT CO₂ and CH₄ retrieval algorithm products with
1125 measurements from the TCCON, *Atmos. Meas. Tech.*, 7, 1723–1744, 2014.



- 1126 Dlugokencky, E. J., L. Bruhwiler, J. W. C. White, L. K. Emmons, P. C. Novelli, S. A. Montzka, K. A. Massie, P. M.
1127 Lang, A. M. Croswell, J. B. Miller and L. V. Gatti, Observational constraints on recent increases in the
1128 atmospheric CH₄ burden, *Geophys. Res. Lett.*, 36, L18803, 2009.
- 1129 Dlugokencky, E. J., E. G. Nisbet, R. Fisher and D. Lowry, Global atmospheric methane: budget, changes and
1130 dangers, *Phil. Trans. Roy. Soc. A* 369, no. 1943, 2058-2072, 2011.
- 1131 Dlugokencky, E., Lang, P. M., Croswell, A. M., Masarie, K. A., and Croswell, M. J.: Atmospheric methane dry-air
1132 mole fractions from the NOAA ESRL carbon cycle cooperative global air sampling network: 1988–2012,
1133 version: 2013-06-18, <ftp://ftp.cmdl.noaa.gov/ccg/ch4/flask/surface>, 2013.
- 1134 European Commission, Joint Research Centre, and Netherlands Environmental Assessment Agency, Emission
1135 database for global atmospheric research (EDGAR), <http://edgar.jrc.ec.europa.eu>, Release version 4.2, 2011.
- 1136 Fishman, J., L. et al., The United States' next generation of atmospheric composition and coastal ecosystem
1137 measurements: NASA's Geostationary Coastal and Air Pollution Events (GEO-CAPE) Mission, BAMS, doi:
1138 10.1175/BAMS-D-11-00201.1, 2012.
- 1139 Frankenberg, C., U. Platt, and T. Wagner. Iterative maximum a posteriori (IMAP)-DOAS for retrieval of strongly
1140 absorbing trace gases: Model studies for CH₄ and CO₂ retrieval from near infrared spectra of SCIAMACHY
1141 onboard ENVISAT, *Atmos. Chem. Phys.*, 5, 9–22, 2005
- 1142 Frankenberg, C., Meirink, J. F., Bergamaschi, P., Goede, A. P. H., Heimann, M., Körner, S., Platt, U., van Weele,
1143 M., and Wagner, T.: Satellite cartography of atmospheric methane from SCIAMACHY on board ENVISAT:
1144 Analysis of the years 2003 and 2004, *J. Geophys. Res.*, 111, D07303, 2006.
- 1145 Frankenberg, C., I. Aben, P. Bergamaschi, E. J. Dlugokencky, R. van Hees, S. Houweling, P. van der Meer, R. Snel,
1146 P. Tol, Global column averaged methane mixing ratios from 2003 to 2009 as derived from SCIAMACHY:
1147 Trends and variability, *J. Geophys. Res.*, 116, D04302, 2011.
- 1148 Frankenberg, C., et al., Airborne methane remote measurements reveal heavy-tail flux distribution in the Four
1149 Corners region, *PNAS*, in press, 2016.
- 1150 Fraser, A., et al., Estimating regional methane surface fluxes: the relative importance of surface and GOSAT mole
1151 fraction measurements, *Atmos. Chem. Phys.*, 13, 5697-5713, 2013.
- 1152 Fraser, A., et al. Estimating regional fluxes of CO₂ and CH₄ using space-borne observations of XCH₄:XCO₂,
1153 *Atmos. Chem. Phys.*, 14, 12883–12895, 2014.
- 1154 Ganesan, A.L., et al., Characterization of uncertainties in atmospheric trace gas inversions using hierarchical
1155 Bayesian methods, *Atmos. Chem. Phys.*, 14, 3855–3864, 2014.
- 1156 Ganesan, A.L., A. J. Manning, A. Grant, D. Young, D. E. Oram, W. T. Sturges, J. B. Moncrieff, and S. O'Doherty,
1157 Quantifying methane and nitrous oxide emissions from the UK and Ireland using a national-scale monitoring
1158 network *Atmos. Chem. Phys.*, 15, 6393–6406, 2015
- 1159 Gloudemans, A.M.S., H. Schrijver, O. P. Hasekamp, and I. Aben, Error analysis for CO and CH₄ total column
1160 retrievals from SCIAMACHY 2.3 μ m spectra, *Atmos. Chem. Phys.*, 8, 3999–4017, 2008.
- 1161 Glumb, R., G. Davis, and C. Lietzke, The TANSO-FTS-2 instrument for the GOSAT-2 Greenhouse Gas Monitoring
1162 Mission, IEEE International Symposium on Geoscience and Remote Sensing IGARSS, 1238-1240, 2014.
- 1163 Harriss, R.C., et al., Using Multi-Scale Measurements to Improve Methane Emission Estimates from Oil and Gas
1164 Operations in the Barnett Shale Region, Texas, *Environ. Sci. Technol.* 49, 7524–7526, 2015.
- 1165 Hartmann, D.L., et al., Observations: atmosphere and surface. In: *Climate Change 2013: The Physical Science
1166 Basis. Contribution of Working Group I to the Fifth Assessment Report of the Intergovernmental Panel on
1167 Climate Change* [Stocker, T.F., D. Qin, G.-K. Plattner, M. Tignor, S.K. Allen, J. Boschung, A. Nauels, Y. Xia,
1168 V. Bex and P.M. Midgley (eds.)]. Cambridge University Press, Cambridge, United Kingdom and New York,
1169 NY, USA, 2013.
- 1170 Heald, C., Jacob, D., Jones, D., Palmer, P., Logan, J., Streets, D., Sachse, G., Gille, J., Hoffman, R., and Nehr Korn,
1171 T.: Comparative inverse analysis of satellite (MOPITT) and aircraft (TRACE-P) observations to estimate
1172 Asian sources of carbon monoxide, *J. Geophys. Res.*, 109, D23306, 2004.
- 1173 Henne, S., et al. (2016), Validation of the Swiss methane emission inventory by atmospheric observations and
1174 inverse modelling, *Atmos. Chem. Phys.*, 16, 3683–3710.
- 1175 Henze, D. K., A. Hakami, and J. H. Seinfeld, Development of the adjoint of GEOS-Chem, *Atmos. Chem. Phys.*, 7,
1176 2413–2433, 2007.
- 1177 Herbin, H., L. C.-Labonne, and P. Dubuisson, Multispectral information from TANSO-FTS instrument – Part
1178 1: Application to greenhouse gases (CO₂ and CH₄) in clear sky conditions, *Atmos. Meas. Tech.*, 6, 3301–3311,
1179 2013.
- 1180 Hiller, R.V., et al. (2016), Anthropogenic and natural methane fluxes in Switzerland synthesized within a spatially
1181 explicit inventory, *Biogeosciences*, 11, 1941–1960.



- 1182 Houweling, S., Kaminski, T., Dentener, F., Lelieveld, J., and Heimann, M.: Inverse modeling of methane sources
 1183 and sinks using the adjoint of a global transport model, *J. Geophys. Res.*, 104, 26137–26160, 1999.
- 1184 Houweling, S., M. Krol, P. Bergamaschi, C. Frankenberg, E. J. Dlugokencky, I. Morino, J. Notholt, V. Sherlock, D.
 1185 Wunch, V. Beck, C. Gerbig, H. Chen, E. A. Kort, T. Röckmann, and I. Aben, A multi-year methane inversion
 1186 using SCIAMACHY, accounting for systematic errors using TCCON measurements, *Atmos. Chem. Phys.*
 1187 14, 3991–4012, 2014.
- 1188 Hulley, G. C., Duren, R. M., Hopkins, F. M., Hook, S. J., Vance, N., Guillevic, P., et al. (2016). High spatial
 1189 resolution imaging of methane and other trace gases with the airborne Hyperspectral Thermal Emission
 1190 Spectrometer (HyTES). *Atmospheric Measurement Techniques Discussions*, 1–32, 2016.
- 1191 IPCC, 2006 IPCC Guidelines for National Greenhouse Gas Inventories, Prepared by the National Greenhouse Gas
 1192 Inventories Programme, Eggleston H.S., Buendia L., Miwa K., Ngara T. and Tanabe K. (eds). IGES, Japan,
 1193 2006.
- 1194 Kaminski, T., Rayner, P. J., Heimann, M., and Enting, I. G.: On aggregation errors in atmospheric transport
 1195 inversions, *J. Geophys. Res.*, 106, 4703, 2001.
- 1196 Karion, A., C. Sweeney, G. Pétron, G. Frost, R. M. Hardesty, J. Kofler, B. R. Miller, T. Newberger, S. Wolter, R.
 1197 Banta, A. Brewer, E. Dlugokencky, P. Lang, S. A. Montzka, R. Schnell, P. Tans, M. Trainer, R. Zamora, and
 1198 S. Conley, Methane emissions estimate from airborne measurements over a western United States natural gas
 1199 field, *Geophys. Res. Lett.*, 40, 4393–4397, doi:10.1002/grl.50811, 2013.
- 1200 Karion, A., et al., Aircraft-Based Estimate of Total Methane Emissions from the Barnett Shale Region, *Environ. Sci.*
 1201 *Technol.*, 49, 8,124–8,131, 2015.
- 1202 Kiemle, C., M. Quatrevalet, G. Ehret, A. Amediek, A. Fix, and M. Wirth, Sensitivity studies for a space-based
 1203 methane lidar mission, *Atmos. Meas. Tech.*, 4, 2195–2211, 2011.
- 1204 Kiemle, C., S. R. Kawa, M. Quatrevalet, and E. V. Browell, Performance simulations for a spaceborne methane lidar
 1205 mission, *J. Geophys. Res. Atmos.*, 119, 4365–4379, 2014.
- 1206 Kirschke, S., P. Bousquet, P. Ciais, M. Saunois, J. G. Canadell, E. J. Dlugokencky, P. Bergamaschi, D. Bergmann,
 1207 D. R. Blake, L. Bruhwiler, P. Cameron-Smith, S. Castaldi, F. Chevallier, L. Feng, A. Fraser, M. Heimann, E.
 1208 L. Hodson, S. Houweling, B. Josse, P. J. Fraser, P. B. Krummel, J.-F. Lamarque, R. L. Langenfelds, C. Le
 1209 Quere, V. Naik, S. O'Doherty, P. I. Palmer, I. Pison, D. Plummer, B. Poulter, R. G. Prinn, M. Rigby, B.
 1210 Ringeval, M. Santini, M. Schmidt, D. T. Shindell, I. J. Simpson, R. Spahni, L. P. Steele, S. A. Strode, K. Sudo,
 1211 S. Szopa, G. R. van der Werf, A. Voulgarakis, M. van Weele, R. F. Weiss, J. E. Williams, and G. Zeng, Three
 1212 decades of global methane sources and sinks, *Nature Geosci.*, 6(10), 813–823, 10.1038/ngeo1955, 2013.
- 1213 Kleipool, Q.L., R.T. Jongma, A.M.S. Gloudemans, H. Schrijver, G.F. Lichtenberg, R.M. van Hees, A.N. Maurellis,
 1214 R.W.M. Hoogeveen, In-flight proton-induced radiation damage to SCIAMACHY's extended-wavelength
 1215 InGaAs near-infrared detectors, *Infrared Physics & Technology*, 50, 30–37, 2007.
- 1216 Kort, E. A., J. Eluszkiewicz, B. B. Stephens, J. B. Miller, C. Gerbig, T. Nehr Korn, B. C. Daube, J. O. Kaplan, S.
 1217 Houweling, and S. C. Wofsy, Emissions of CH₄ and N₂O over the United States and Canada based on a
 1218 receptor-oriented modeling framework and COBRA-NA atmospheric observations, *Geophys. Res. Lett.*, 35,
 1219 L18808, doi:10.1029/2008GL034031, 2008.
- 1220 Kort, E. A., C. Frankenberg, K. R. Costigan, R. Lindenmaier, M. K. Dubey, and D. Wunch, Four corners: The
 1221 largest US methane anomaly viewed from space, *Geophys. Res. Lett.*, 41, 6898–6903, 2014.
- 1222 Krings, T., K. Gerilowski, M. Buchwitz, M. Reuter, A. Tretner, J. Erzinger, D. Heinze, U. Pfluger, J.P. Burrows,
 1223 and H. Bovensmann, MAMAP – a new spectrometer system for column-averaged methane and carbon dioxide
 1224 observations from aircraft: retrieval algorithm and first inversions for point source emission rates, *Atmos.*
 1225 *Meas. Tech.*, 4, 1735–1758, 2011.
- 1226 Krings, T., K. Gerilowski, M. Buchwitz, J. Hartmann, T. Sachs, J. Erzinger, J.P. Burrows, and H. Bovensmann,
 1227 Quantification of methane emission rates from coal mine ventilation shafts using airborne remote sensing data,
 1228 *Atmos. Meas. Tech.*, 6, 151–166, 2013.
- 1229 Kulawik, S., et al., Consistent evaluation of ACOS-GOSAT, BESD-SCIAMACHY, CarbonTracker, and MACC
 1230 through comparisons to TCCON, *Atmos. Meas. Tech.*, 9, 683–709, 2016.
- 1231 Kuze, A., H. Suto, M. Nakajima, and T. Hamazaki, Thermal and near infrared sensor for carbon observation
 1232 Fourier-transform spectrometer on the Greenhouse Gases Observing Satellite for greenhouse gases monitoring,
 1233 *Appl. Opt.*, 48, 6,716–6,733, 2009.
- 1234 Kuze, A., et al., Update on GOSAT TANSO-FTS performance, operations, and data products after more than six
 1235 years in space, *Atmos. Meas. Tech. Discuss.*, doi:10.5194/amt-2015-333, 2016



- 1236 Lyon, D. R., Zavala-Araiza, D., Alvarez, R. A., Harriss, R., Palacios, V., Lan, X., Talbot, R., Lavoie, T., Shepson,
 1237 P., Yacovitch, T. I., et al. Constructing a spatially resolved methane emission inventory for the Barnett Shale
 1238 region. *Environ. Sci. Technol.*, 8147–8157, 2015.
- 1239 Maasakkers, J.D., et al., A gridded national inventory of US methane emissions, submitted to *Environ. Sci.*
 1240 *Technol.*, 2016.
- 1241 Marais, E. A., D. J. Jacob, K. Wecht, C. Lerot, L. Zhang, K. Yu, T. P. Kurosu, K. Chance, and B.
 1242 Sauvage, Anthropogenic emissions in Nigeria and implications for ozone air quality: a view from
 1243 space, *Atmos. Environ.*, 99, 32–40, 2014.
- 1244 Marchese, A. J., Vaughn, T. L., Zimmerle, D. J., Martinez, D. M., Williams, L. L., Robinson, A. L., Mitchell, A. L.,
 1245 Subramanian, R., Tkacik, D. S., Roscioli, J. R., et al. (2015). Methane emissions from United States natural gas
 1246 gathering and processing, *Environ. Sci. Technol.*, 49, 10,718–10,727, 2015.
- 1247 Melton, J. R., R. Wania, E. L. Hodson, B. Poulter, B. Ringeval, R. Spahni, T. Bohn, C. A. Avis, D. J. Beerling, G.
 1248 Chen, A. V. Eliseev, S. N. Denisov, P. O. Hopcroft, D. P. Lettenmaier, W. J. Riley, J. S. Singarayer, Z. M.
 1249 Subin, H. Tian, S. Zurcher, V. Brovkin, P. M. vanBodegom, T. Kleinen, Z. C. Yu, and J. O. Kaplan, Present
 1250 state of global wetland extent and wetland methane modelling: conclusions from a model inter-comparison
 1251 project (WETCHIMP), *Biogeosciences*, 10 (2), 753–788, 2013.
- 1252 Miller, S.M., S. C. Wofsy, A. M. Michalak, E. A. Kort, A. E. Andrews, S. C. Biraud, E. J. Dlugokencky, J.
 1253 Eluskiewicz, M. L. Fisher, G. Janssens-Maenhout, B. R. Miller, J. B. Miller, S. A. Montzka, T. Nehrkorn, and
 1254 C. Sweeney, Anthropogenic emissions of methane in the US, *PNAS*, doi:10.1073/pnas.1314392110, 2013.
- 1255 Miller, S.M., A.M. Michalak, and P. J. Levi, Atmospheric inverse modeling with known physical bounds: an
 1256 example from trace gas emissions, *Geosci. Model Dev.*, 7, 303–315, 2014.
- 1257 Minschwaner, K., and G.L. Manney, Derived methane in the stratosphere and lower mesosphere from Aura
 1258 Microwave Limb Sounder measurements of nitrous oxide, water vapor, and carbon monoxide, *J Atmos Chem.*,
 1259 71:253–267, 2014.
- 1260 Mitchell, A.L., et al. Measurements of Methane Emissions from Natural Gas Gathering Facilities and Processing
 1261 Plants: Measurement Results, *Environ. Sci. Technol.*, 49, 3,219–3,227, 2015.
- 1262 Monteil, G., S. Houweling, A. Butz, S. Guerlet, D. Schepers, O. Hasekamp, C. Frankenberg, R. Scheepmaker, I.
 1263 Aben, and T. Röckmann, Comparison of CH₄ inversions based on 15 months of GOSAT and SCIAMACHY
 1264 observations, *J. Geophys. Res. Atmos.*, 118, doi:10.1002/2013JD019760, 2013.
- 1265 Myhre, G., et al., Anthropogenic and Natural Radiative Forcing. In: *Climate Change 2013: The Physical Science*
 1266 *Basis. Contribution of Working Group I to the Fifth Assessment Report of the Intergovernmental Panel on*
 1267 *Climate Change* [Stocker, T.F., D. Qin, G.-K. Plattner, M. Tignor, S.K. Allen, J. Boschung, A. Nauels, Y. Xia,
 1268 V. Bex and P.M. Midgley (eds.)]. Cambridge University Press, Cambridge, United Kingdom and New York,
 1269 NY, USA, 2013.
- 1270 Ostler, A., et al., The imprint of stratospheric transport on column-averaged methane, *Atmos. Chem. Phys. Discuss.*,
 1271 15, 20395–20447, 2015
- 1272 Pandey, S., S. Houweling, M. Krol, I. Aben, and T. Röckmann, On the use of satellite-derived CH₄ :CO₂ columns
 1273 in a joint inversion of CH₄ and CO₂ fluxes, *Atmos. Chem. Phys.*, 15, 8615–8629, 2015
- 1274 Parker, R., H. Boesch, A. Cougan, A. Fraser, L. Feng, P. I. Palmer, J. Messerschmidt, N. Deutscher, D. W. T.
 1275 Griffith, J. Notholt, P. O. Wennberg and D. Wunch, Methane observations from the Greenhouse Gases
 1276 Observing SATellite: Comparison to ground-based TCCON data and model calculations, *Geophys. Res. Lett.*,
 1277 38, L15807, 2011.
- 1278 Parker, R.J., et al., Assessing 5 years of GOSAT Proxy XCH₄ data and associated uncertainties, *Atmos. Meas.*
 1279 *Tech.*, 8, 4785–4801, 2015.
- 1280 Patra, P.K., et al., TransCom model simulations of CH₄ and related species: linking transport, surface flux and
 1281 chemical loss with CH₄ variability in the troposphere and lower stratosphere, *Atmos. Chem. Phys.*, 11, 12813–
 1282 12837, 2011.
- 1283 Peischl, J, et al., Quantifying sources of methane using light alkanes in the Los Angeles basin, California, *J.*
 1284 *Geophys. Res.*, 118, 4974–4990. 2013.
- 1285 Peischl, J., et al., Quantifying atmospheric methane emissions from the Haynesville, Fayetteville, and northeastern
 1286 Marcellus shale gas production regions. *J. Geophys. Res.*, 120, 2119–2139, 2015.
- 1287 Peischl, J., A. Karion, C. Sweeney, E. A. Kort, M. L. Smith, A. R. Brandt, T. Yeskoo, K. C. Aikin, S. A. Conley, A.
 1288 Gvakharia, M. Trainer, S. Wolter and T. B. Ryerson, Quantifying atmospheric methane emissions from oil and
 1289 natural gas production in the Bakken shale region of North Dakota, *J. Geophys. Res.*,
 1290 DOI: 10.1002/2015JD024631, 2016.



- 1291 Polonsky, L.N., et al., Performance of a geostationary mission, geoCARB, to measure CO₂, CH₄ and CO column-
1292 averaged concentrations, *Atmos. Meas. Tech.*, 7, 959–981, 2014.
- 1293 Prather, M.J., Timescales in atmospheric chemistry: Theory, GWPs for CH₄ and CO, and runaway growth,
1294 *Geophys. Res. Lett.*, 23, 2597–2600 1996.
- 1295 Prather, M. J., C. D. Holmes, and J. Hsu: Reactive greenhouse gas scenarios: Systematic exploration of uncertainties
1296 and the role of atmospheric chemistry, *Geophys. Res. Lett.*, 39, L09803, doi:10.1029/2012GL051440, 2012.
- 1297 President's Climate Action Plan: Strategy to Reduce Methane Emissions,
1298 http://www.whitehouse.gov/sites/default/files/strategy_to_reduce_methane_emissions_2014-03-28_final.pdf,
1299 2014.
- 1300 Rayner, P.J., S.R. Utembe, and S. Crowell, Constraining regional greenhouse gas emissions using geostationary
1301 concentration measurements: a theoretical study, *Atmos. Meas. Tech.*, 7, 3285–3293, 2014.
- 1302 Remer, L.A., S. Mattoo, R. C. Levy, A. Heidinger, R. B. Pierce, and M. Chin, Retrieving aerosol in a cloudy
1303 environment: aerosol product availability as a function of spatial resolution, *Atmos. Meas. Tech.*, 5, 1823–
1304 1840, 2012
- 1305 Roberts, D.A., Bradley, E.S., Cheung, R., Leifer, I., Dennison, P.E. and Margolis, J.S., Mapping methane emissions
1306 from a marine geological seep source using imaging spectrometry. *Remote Sensing of Environment*, 114, 592–
1307 606, 2010.
- 1308 Rodgers, C.D.: *Inverse Methods for Atmospheric Sounding*, World Scientific Publishing Co., Singapore, 2000.
- 1309 Saad, K.M., Derivation of tropospheric methane from TCCON CH₄ and HF total column observations, *Atmos.*
1310 *Meas. Tech.*, 7, 2907–2918, 2014.
- 1311 Schepers, D., Guerlet, S., Butz, A., Landgraf, J., Frankenberg, C., Hasekamp, O., Blavier, J.-F., Deutscher, N.M.,
1312 Griffith, D.W.T., Hase, F., Kyro, E., Morino, I., Sherlock, V., Sussmann, R., and Aben, I., Methane retrievals
1313 from Greenhouse Gases Observing Satellite (GOSAT) shortwave infrared measurements: Performance
1314 comparison of proxy and physics retrieval algorithms, *J. Geophys. Res.*, 117, D10307,
1315 doi:10.1029/2012JD017549, 2012.
- 1316 Schneising, O., J. P. Burrows, R. R. Dickerson, M. Buchwitz, M. Reuter, and H. Bovensmann, Remote sensing of
1317 fugitive methane emissions from oil and gas production in North American tight geologic formations, *Earth's*
1318 *Future*, 2, 548–558, 2014.
- 1319 Shephard, M.W., et al., TES ammonia retrieval strategy and global observations of the spatial and seasonal
1320 variability of ammonia, *Atmos. Chem. Phys.*, 11, 10743–10763, 2011.
- 1321 Shephard, M.W., and K.E. Cady-Pereira, Cross-track Infrared Sounder (CrIS) satellite observations of tropospheric
1322 ammonia, *Atmos. Meas. Tech.*, 8, 1323–1336, 2015.
- 1323 Spahni, R., et al., Constraining global methane emissions and uptake by ecosystems, *Biogeosciences*, 8, 1643–1665,
1324 2011.
- 1325 Streets, D., T. Canty, G. Carmichael, B. de Foy, R. Dickerson,, B. Duncan, D. Edwards, J. Haynes, D. Henze, M.
1326 Houyoux, D. Jacob, N. Krotkov, L. Lamsal, Y. Liu, Z. Lu, R. Martin, G. Pfister, R. Pinder, R. Salawitch, and
1327 K. Wecht, Emissions estimation from satellite retrievals: A review of current capability, *Atmos. Environ.*, 77,
1328 1011–1042, 2013.
- 1329 Thompson, D.R., Leifer, I., Bovensmann, H., Eastwood, M., Fladeland, M., Frankenberg, C., Gerilowski, K., Green,
1330 R.O., Kratwurst, S., Krings, T. and Luna, B., Real-time remote detection and measurement for airborne
1331 imaging spectroscopy: a case study with methane. *Atmospheric Measurement Techniques*, 8, 4383–4397, 2015.
- 1332 Thorpe, A.K., C. Frankenberg, A.D. Aubrey, D.A. Roberts, A.A. Nottrott, T.A. Rahn, J.A. Sauer, M.K. Dubey, K.R.
1333 Costigan, C. Arata, A.M. Steffke, S. Hills, C. Haselwimmer, D. Charlesworth, C.C. Funk, R.O. Green, S.R.
1334 Lundeen, J.W. Boardman, M.L. Eastwood, C.M. Sarture, S.H. Nolte, I.B. Mccubbin, D.R. Thompson, and J.P.
1335 McFadden, Mapping methane concentrations from a controlled release experiment using the next generation
1336 airborne visible/infrared imaging spectrometer (AVIRIS-NG), *Remote Sensing of Environment*, 179, 104–115,
1337 2016.
- 1338 Tratt, D.M., Buckland, K.N., Hall, J.L., Johnson, P.D., Keim, E.R., Leifer, I., Westberg, K. and Young, S.J., 2014.
1339 Airborne visualization and quantification of discrete methane sources in the environment, *Remote Sensing of*
1340 *Environment*, 154, 74–88, 2014.
- 1341 Turner, A.J. and D.J. Jacob, Balancing aggregation and smoothing errors in inverse models, *Atmos. Chem. Phys.*,
1342 15, 7039–7048, 2015.
- 1343 Turner, A.J., D.J. Jacob, K.J. Wecht, J.D. Maasackers, E. Lundgren, A.E. Andrews, S.C. Biraud, H. Boesch, K.W.
1344 Bowman, N.M. Deutscher, M.K. Dubey, D.W.T. Griffith, F. Hase, A. Kuze, J. Notholt, H. Ohyama, R. Parker,
1345 V.H. Payne, R. Sussmann, C. Sweeney, V.A. Velazco, T. Warneke, P.O. Wennberg, and D.



- 1346 Wunch, Estimating global and North American methane emissions with high spatial resolution using GOSAT
1347 satellite data, *Atmos. Chem. Phys.*, 15, 7049-7069, 2015.
- 1348 Turner, A.J., D.J. Jacob, J. Benmergui, S.C. Wofsy, J.D. Maasakkers, A. Butz, O. Hasekamp, S.C. Biraud, and E.
1349 Duglokencky, A large increase in US methane emissions over the past decade inferred from satellite data,
1350 *Geophys. Res. Lett.*, 43, doi:10.1029/2016GL067987, 2016.
- 1351 US EPA, Inventory of U.S. greenhouse gas emissions and sinks: 1990-2012,
1352 <https://www3.epa.gov/climatechange/ghgemissions/usinventoryreport.html>, 2016.
- 1353 Van Damme, M., R. J. Wichink Kruit, M. Schaap, L. Clarisse, C. Clerbaux, P.-F. Coheur, E. Dammers, A. J.
1354 Dolman, and J. W. Erisman, Evaluating 4 years of atmospheric ammonia (NH₃) over Europe using IASI
1355 satellite observations and LOTOS-EUROS model results, *J. Geophys. Res.*, 119, 9549–9566, 2014.
- 1356 Veeffkind, J.P., Aben, I., McMullan, K., Forster, H., de Vries, J., Otter, G., Claas, J., Eskes, H.J., de Haan, J.F.,
1357 Kleipool, Q., van Weele, M., Hasekamp, O., Hoogeveen, R., Landgraf, J., Snel, R., Tol, P., Ingmann, P.,
1358 Voors, R., Kruizinga, B., Vink, R., Visser, H., and Levelt, P.F., TROPOMI on the ESA Sentinel-5 Precursor: A
1359 GMES mission for global observations of the atmospheric composition for climate, air quality and ozone layer
1360 applications, *Remote Sensing of Environment* 120, 70-83, 2012.
- 1361 Von Clarmann, T., et al., Retrieval of temperature, H₂O, O₃, HNO₃, CH₄, N₂O, ClONO₂ and ClO from MIPAS
1362 reduced resolution nominal mode limb emission measurements, *Atmos. Meas. Tech.*, 2, 159–175, 2009.
- 1363 Voulgarakis, A., et al., Analysis of present day and future OH and methane lifetime in the ACCMIP simulations,
1364 *Atmos. Chem. Phys.*, 13, 2563–2587, 2013.
- 1365 Wang, H., D.J. Jacob, M. Kopacz, D.B.A. Jones, P. Suntharalingam, J.A. Fisher, R. Nassar, S. Pawson, and J.E.
1366 Nielsen, Error correlation between CO₂ and CO as constraint for CO₂ flux inversions using satellite
1367 data, *Atmos. Chem. Phys.*, 9, 7,313-7,323, 2009.
- 1368 Wang, Y.-P., and S.T. Bentley, Development of a spatially explicit inventory of methane emissions from Australia
1369 and its verification using atmospheric concentration data, *Atmos. Environ.*, 36, 4,985-4,975, 2002.
- 1370 Wecht, K. J., D. J. Jacob, S. C. Wofsy, E. A. Kort, J. R. Worden, S. S. Kulawik, D. K. Henze, M. Kopacz, and V. H.
1371 Payne, Validation of TES methane with HIPPO aircraft observations: implications for inverse modeling of
1372 methane sources, *Atmos. Chem. Phys.*, 12, 1823–1832, 2012.
- 1373 Wecht, K.J., D.J. Jacob, C. Frankenberg, Z. Jiang, and D.R. Blake, Mapping of North America methane emissions
1374 with high spatial resolution by inversion of SCIAMACHY satellite data, *J. Geophys. Res.*, 119,
1375 DOI: 10.1002/2014JD021551, 2014a.
- 1376 Wecht, K.J., D.J. Jacob, M.P. Sulprizio, G.W. Santoni, S.C. Wofsy, R. Parker, H. Bösch, and J.R. Worden, Spatially
1377 resolving methane emissions in California: constraints from the CalNex aircraft campaign and from present
1378 (GOSAT, TES) and future (TROPOMI, geostationary) satellite observations, *Atm. Chem. Phys.*, 14, 8175-
1379 8184, 2014b.
- 1380 Wennberg, P.O., et al., On the sources of methane to the Los Angeles atmosphere, *Environ. Sci. Technol.*, 46, 9282-
1381 9289, 2012.
- 1382 Wofsy, S. C.: HIAPER Pole-to-Pole Observations (HIPPO): finegrained, global-scale measurements of climatically
1383 important atmospheric gases and aerosols, *Philos. T. Roy. Soc. A*, 369, 2073–2086, 2011.
- 1384 Worden, H.M., M.N. Deeter, D.P. Edwards, J.C. Gille, and J.R. Drummond, Observations of near-surface carbon
1385 monoxide from space using MOPITT multispectral retrievals, *J. Geophys. Res.*, 115, D18314, 2010.
- 1386 Worden, J., S. Kulawik, C. Frankenberg, V. Payne, K. Bowman, K. Cady-Peirara, K. Wecht, J.-E. Lee, and D.
1387 Noone, Profiles of CH₄, HDO, H₂O, and N₂O with improved lower tropospheric vertical resolution from Aura
1388 TES radiances, *Atmos. Meas. Tech.*, 5, 397–411, 2012.
- 1389 Worden, J., et al., CH₄ and CO distributions over tropical fires during October 2006 as observed by the Aura TES
1390 satellite instrument and modeled by GEOS-Chem, *Atmos. Chem. Phys.*, 13, 3679–3692, 2013.
- 1391 Worden, J.R., et al., Quantifying lower tropospheric methane concentrations using GOSAT near-IR and TES
1392 thermal IR measurements, *Atmos. Meas. Tech.*, 8, 3433–3445, 2015
- 1393 Wunch, D., G. C. Toon, J-F. L. Blavier, R. A. Waschenfelder, J. Notholt, B. J. Connor, D. W. T. Griffith, V.
1394 Sherlock and P. O. Wennberg, The Total Carbon Column Observing Network, *Phil. Trans. R. Soc. A*, 369,
1395 2087-2112, 2011.
- 1396 Xi, X., V. Natraj, R. L. Shia, M. Luo, Q. Zhang, S. Newman, S. P. Sander, and Y. L. Yung, Simulated retrievals for
1397 the remote sensing of CO₂, CH₄, CO, and H₂O from geostationary orbit, *Atmos. Meas. Tech.*, 8, 4817–4830,
1398 2015.
- 1399 Xiao, Y, D.J. Jacob, J. Wang, J.A. Logan, P.I. Palmer, P. Suntharalingam, R.M. Yantosca, G.W. Sachse, D.R. Blake,
1400 D.G. Streets, Constraints on Asian and European sources of methane from CH₄-C₂H₆-CO correlations in Asian
1401 outflow, *J. Geophys. Res.*, 109, D15S16, 2004.



- 1402 Xiong, X., C. Barnet, E. Maddy, C. Sweeney, X. Liu, L. Zhou, and M. Goldberg, Characterization and validation of
1403 methane products from the Atmospheric Infrared Sounder (AIRS), *J. Geophys. Res.*, 113, G00A01,
1404 doi:10.1029/2007JD000500, 2008.
- 1405 Xiong, X., C. Barnet, E. S. Maddy, A. Gambacorta, T. S. King, and S. C. Wofsy, Mid-upper tropospheric methane
1406 retrieval from IASI and its validation, *Atmos. Meas. Tech.*, 6, 2255-2265, doi:10.5194/amt-6-2255-2013, 2013.
- 1407 Zavala-Araiza, D., et al., Toward a functional definition of methane super-emitters: application to natural gas
1408 production sites, *Environ. Sci. Technol.*, 49, 8,167-8,174, 2015.
- 1409 Zhang, L., D. J. Jacob, X. Liu, J. A. Logan, K. Chance, A. Eldering, and B. R. Bojkov, Intercomparison methods for
1410 satellite measurements of atmospheric composition: application to tropospheric ozone from TES and OMI,
1411 *Atmos. Chem. Phys.*, 10, 4,725-4,739, 2010.
- 1412 Zhao, C., A.E. Andrews, L. Bianco, J. Eluszkiewicz, A. Hirsch, C. MacDonald, T. Nehrkorn, and M.L. Fischer,
1413 Atmospheric inverse estimates of methane emissions from Central California, *J. Geophys. Res.*, 114, D16302,
1414 2009.
- 1415 Zhu, L., D. K. Henze, K. E. Cady-Pereira, M. W. Shephard, M. Luo, R. W. Pinder, J. O. Bash, and G.-R. Jeong,
1416 Constraining U.S. ammonia emissions using TES remote sensing observations and the GEOS-Chem adjoint
1417 model, *J. Geophys. Res.*, 118, 3355–3368, 2013.
- 1418 Zoogman, P., D.J. Jacob, K. Chance, X. Liu, A. Fiore, M. Lin, K. Travis, Monitoring high-ozone events in the US
1419 Intermountain West using TEMPO geostationary satellite observations, *Atmos. Chem. Phys.*, 14, 6261-6271,
1420 2014.
- 1421

1422 **Table 1.** Satellite instruments for measuring tropospheric methane^a

Instrument	Agency ^b	Data period	Overpass time [local]	Fitting window [nm] (spectral resolution)	Pixel size [km ²] ^c	Coverage ^d	Precision ^e	Reference
<i>Low Earth Orbit^f</i>								
<i>Solar backscatter</i>								
SCIAMACHY	ESA	2003-2012	10:00	1630-1670 (1.4) ^g	30×60	6 days	1.5 % ^h	Frankenberg et al. (2006)
GOSAT ⁱ	JAXA	2009-	13:00	1630-1700 (0.06)	10×10	3 days ^j	0.7 %	Kuze et al. (2016)
TROPOMI	ESA	2016-	13:30	2310-2390 (0.25)	7×7	1 day	0.6%	Butz et al. (2012)
GHGSat	GHGSat, Inc.	2016-	09:30	1600-1700 (0.1)	0.05×0.05 ^k	12×12 km ² grid ^l	1-5%	Footnote ^m
GOSAT-2	JAXA	2018-	13:00	1630-1700, 2330-2380 (0.06)	10×10	3 days ^j	0.4%	Glumb et al. (2014)
CarbonSat	ESA	proposed		1590-1680 (0.3)	2×2	5-10 days	0.4%	Buchwitz et al. (2013)
<i>Thermal emission</i>								
IMG	MITI	1996-1997	10:30/22:30	7100-8300 (0.7)	8×8	along track	4%	Clerbaux et al. (2003)
AIRS	NASA	2002-	13:30/01:30	6200-8200 (7)	45×45	0.5 days	1.5 %	Xiong et al. (2008)
TES	NASA	2004-2011	13:30/01:30	7580-8850 (0.8)	5×8	along track	1.0 %	Worden et al. (2012)
IASI	EUMETSAT	2007-	09:30/21:30	7100-8300 (1.5)	12×12	0.5 days	1.2 %	Xiong et al. (2013)
CrIS	NOAA	2011-	13:30/01:30	7300-8000 (1.6)	14×14	0.5 days	1.5%	Barnet et al. (2014)
<i>Active (lidar)</i>								
MERLIN	DLR/CNES	2020-	13:30/01:30	1645.552/1645.846 ⁿ	pencil	along track	1.0% ^o	Kiemle et al. (2011, 2014)
<i>Geostationary</i>								
GEO-CAPE ^p	NASA	proposed	continuous	2300 nm band	4×4 ^q	1 hour ^r	1.0%	Fishman et al. (2012)
GeoFTS	NASA	proposed	continuous	1650 and 2300 nm bands	3×3 ^q	2 hours ^r	<0.2%	Xi et al. (2015)
geoCARB	NASA	proposed	continuous	2300 nm band	4×5 ^q	2-8 hours ^r	1.0%	Polonsky et al. (2014)

1423 ^a Solar occultation and limb instruments measuring methane in the stratosphere are referenced in Sect. 3.2.

1424 ^b ESA = European Space Agency; JAXA = Japan Aerospace Exploration Agency; MITI = Japan Ministry of

1425 International Trade and Industry; NASA = US National Aeronautics and Space Administration; EUMETSAT =

1426 European Organization for the Exploitation of Meteorological Satellites; DLR = German Aerospace Center; CNES =

1427 French National Center for Space Studies. GHGSat, Inc. is a private Canadian company.

1428 ^c At the subsatellite point.

1429 ^d Time required for full global coverage (low Earth orbit) or continental coverage (geostationary orbit). Solar

1430 backscatter and lidar instruments observe the full methane column with near-uniform sensitivity, while thermal

1431 emission instruments are limited to the middle/upper troposphere (Fig. 3). Solar backscatter instruments observe only in

1432 the daytime and over land (except for sunglint observations).

1433 ^e 1- σ uncertainty for single observations.

1434 ^f All in polar sun-synchronous orbit, observing at a fixed time of day (see “overpass time” column).

1435 ^g SCIAMACHY also had a 2.3 μ m band intended for operational methane retrievals (Gloude-mans et al., 2008) but this

1436 was abandoned due to poor detector performance.

1437 ^h Precision for 2003-2005 observations, after which the instrument degraded (Frankenberg et al., 2011). The average

1438 single-observation precision for the 2003-2012 record is 3-5% (Buchwitz et al., 2015).

1439 ⁱ TANSO-FTS instrument aboard the GOSAT satellite. We refer to the instrument in the text as “GOSAT” following

1440 common practice.

1441 ^j Repeated observations at 3 cross-track pixels about 260 km apart and with 260 km along-track separation. GOSAT

1442 can also adjust its pointing to observe specific targets.

1443 ^k GHGSat’s ground sampling distance is 23 m (512 pixels span the 12 km field of view), but imaging resolution is

1444 anticipated to be about 50 m (limited by telescope focus).

1445 ^l With revisit time of 2 weeks.

1446 ^m Unpublished information from GHGSat, Inc. Description of the GHGSat instrument can be found in Brakeboer

1447 (2015).

1448 ⁿ On-line/off-line.

1449 ^o Monthly average along 50-km tracks.

1450 ^p Specifications from the proposed CHRONOS implementation of GEO-CAPE

1451 (<https://www2.acom.ucar.edu/chronos>).

1452 ^q At roughly 30° latitude; the pixel latitudinal dimension increases with latitude.

1453 ^r Over a continental-scale domain.

1454

1455



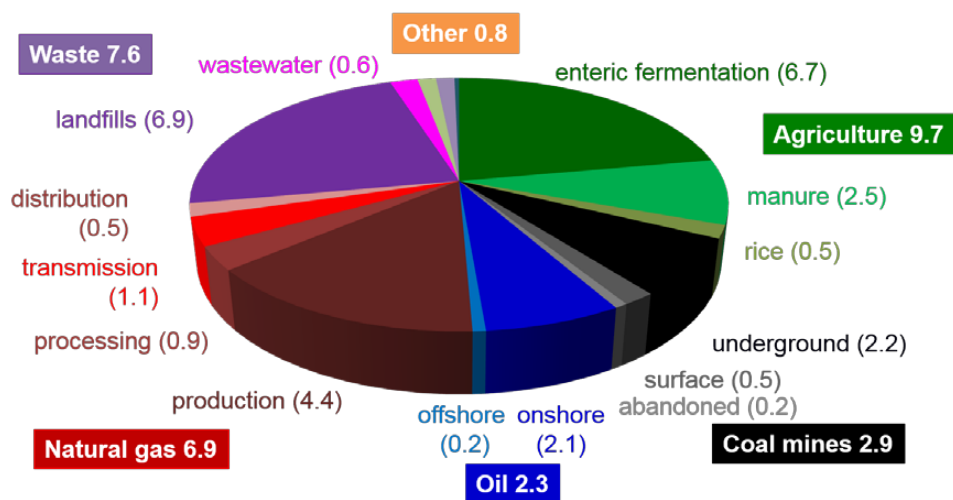
1456 Table 2. Capability for observing regional and point sources of methane from space

1457

Instrument ^a	Regional source quantification ($Q = 72 \text{ tons h}^{-1}$ over $300 \times 300 \text{ km}^2$) ^b	Point source detection threshold ^c (Q_{min} , tons h^{-1})
SCIAMACHY	1 year averaging time	68
GOSAT	1 year averaging time	7.0
TROPOMI	single pass	4.2
GHGSat	NA ^d	0.24 ^e
GOSAT-2	4 months averaging time	4.0
CarbonSat	single pass	0.80
GEO-CAPE, geoCARB	1 hour	4.0
GeoFTS	1 hour	0.8 ^f

1458 ^a See Table 1 for instrument specifications.1459 ^b example of the Barnett Shale region in Northeast Texas (Lyon et al., 2015)1460 ^c For a single observing pass. Detectability scales as Q/U and is given here for a wind speed $U = 5 \text{ km h}^{-1}$.1461 ^d Not applicable. GHGSat has a $12 \times 12 \text{ km}^2$ viewing domain, designed to observe point sources.1462 ^e Assuming 5% precision.1463 ^f Assuming 0.2% precision

1464

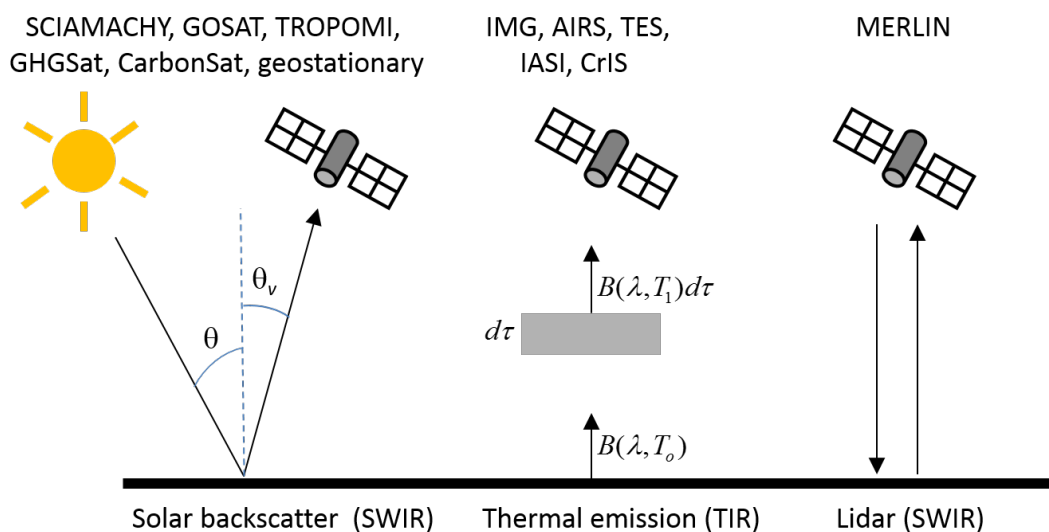


1465
1466
1467
1468
1469

Figure 1. US national emission inventory for methane in 2012 compiled by the US EPA (2016). Units are Tg a⁻¹.



1470



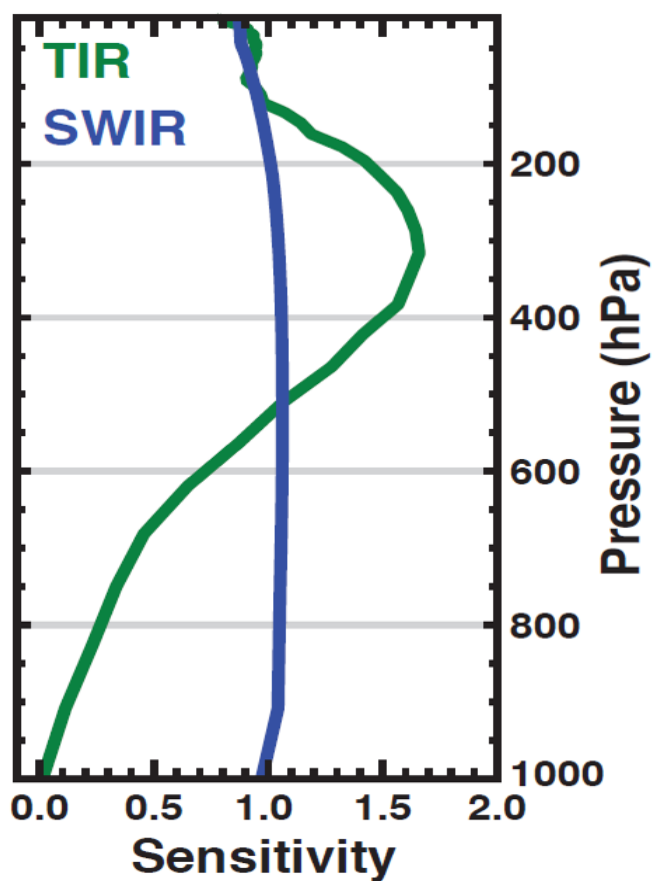
1471

1472

1473 Figure 2. Configurations for observing methane from space in the shortwave infrared (SWIR)
1474 and in the thermal infrared (TIR). Here θ is the solar zenith angle, θ_v is the satellite viewing
1475 angle, $B(\lambda, T)$ is the blackbody function of wavelength λ and temperature T (T_o at the surface, T_1
1476 at the altitude of the emitting methane), and $d\tau$ is an elemental methane optical depth. Satellite
1477 instruments operating in the different configurations are identified in the Figure and listed in
1478 Table 1.
1479

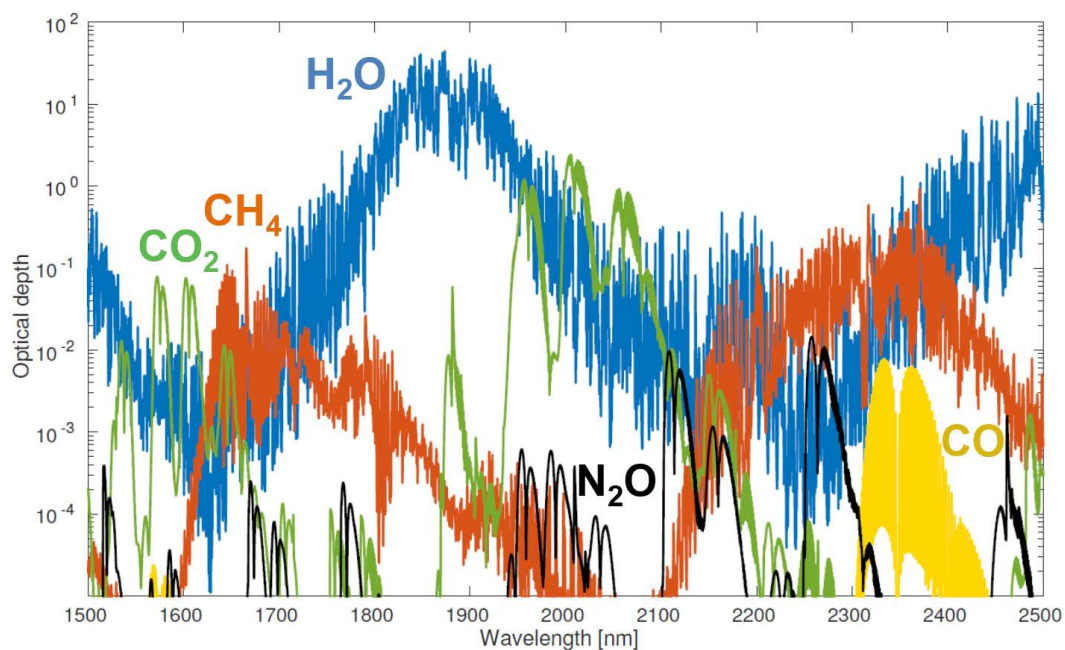


1480
1481



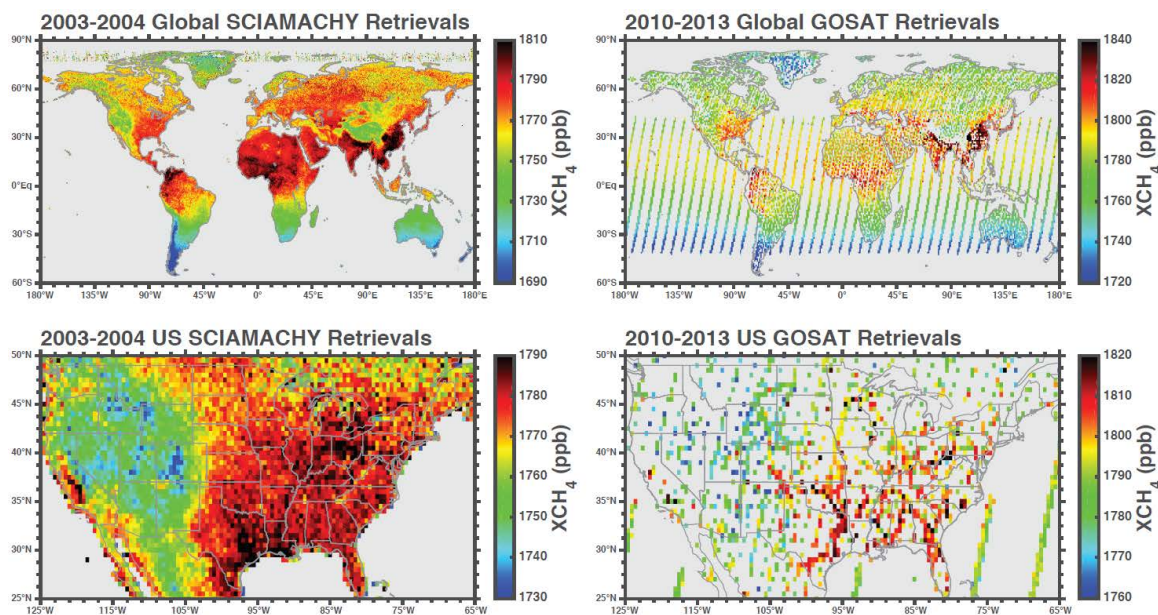
1482
1483
1484
1485
1486
1487
1488

Figure 3. Typical sensitivities as a function of altitude (pressure) for satellite observation of atmospheric methane in the SWIR and in the TIR. The sensitivities are the elements of the averaging kernel vector \mathbf{a} at different pressure levels (Eq. (1)). Adapted from Worden et al. (2015).



1489
1490
1491
1492
1493
1494

Figure 4. Atmospheric optical depths of major trace gases in the spectral region 1.5-2.5 μm . The calculation is for the US Standard Atmosphere (Anderson et al., 1986) with surface concentrations adjusted to 399 ppm CO_2 , 1.9 ppm methane, 330 ppb N_2O , and 80 ppb CO. The line-by-line data are smoothed with a spectral resolution of 0.1 nm (full width at half maximum).

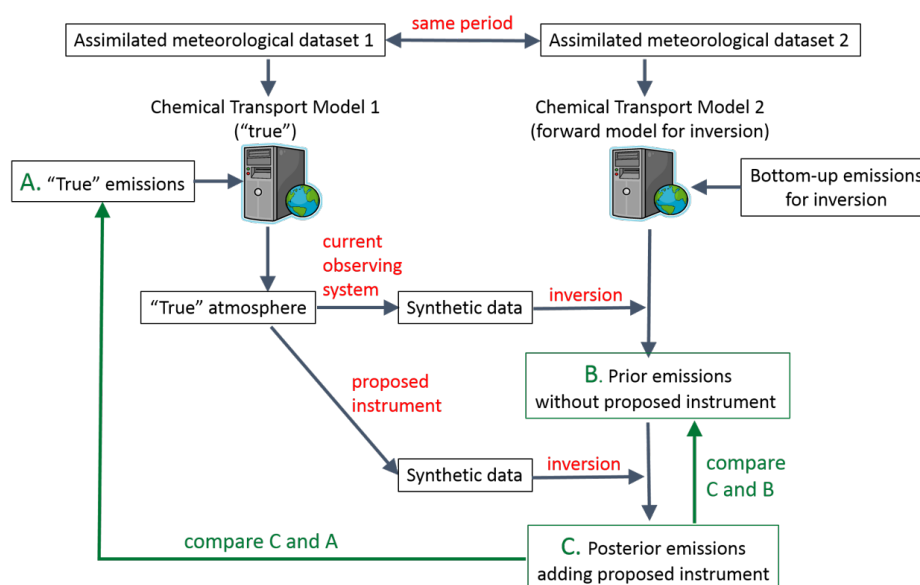


1495
1496
1497
1498
1499
1500
1501
1502
1503
1504
1505

Figure 5. Global and US distributions of methane dry-air column mole fractions (X_{CH_4}) observed by SCIAMACHY and GOSAT. Values are annual means for 2003-2004 (SCIAMACHY) and 2010-2013 (GOSAT), using the CO_2 proxy retrievals from Frankenberg et al. (2011) for SCIAMACHY and Parker et al. (2011) for GOSAT. GOSAT includes observations of sun glint over the oceans. The colorbar is shifted by 30 ppb between the SCIAMACHY and GOSAT panels to account for the global growth of methane from 2003-2004 to 2010-2013. All data are plotted on a $0.5^\circ \times 0.5^\circ$ grid except for the GOSAT global panel where a $1^\circ \times 1^\circ$ grid is used to improve visibility.

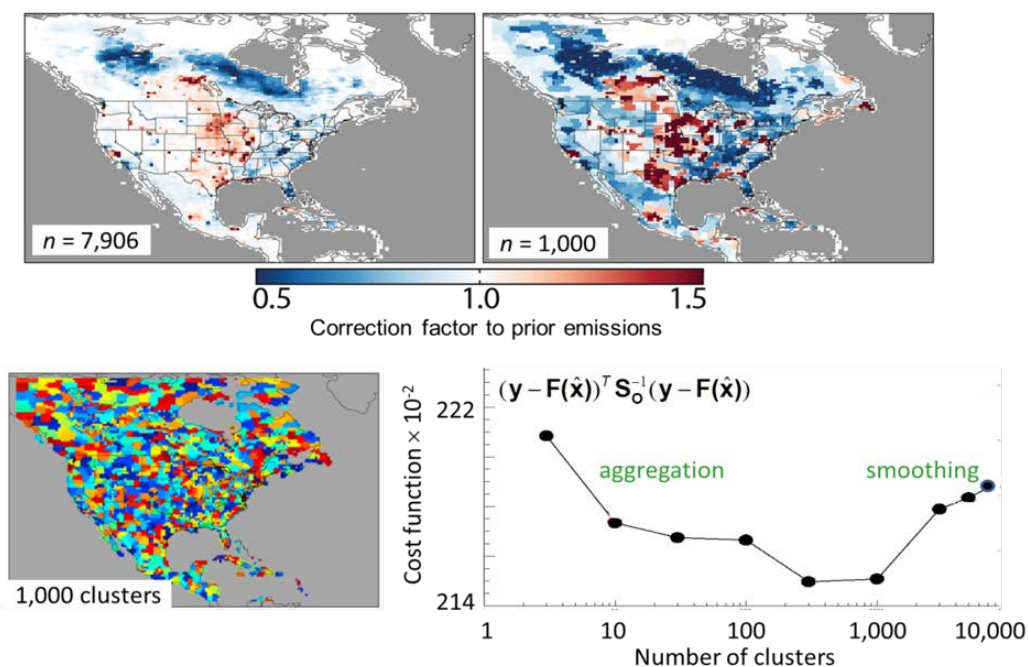


1506



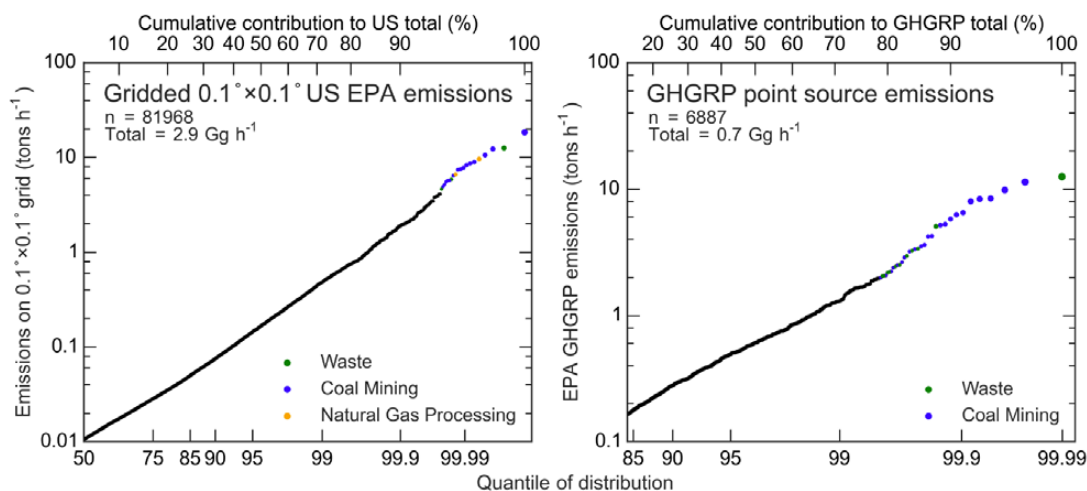
1507
1508
1509
1510
1511
1512
1513

Figure 6. Generic design of an observing system simulation experiment (OSSE) to evaluate the potential of a proposed new atmospheric instrument to improve knowledge of emissions relative to the current observing system.



1514
1515
1516
1517
1518
1519
1520
1521
1522
1523
1524
1525
1526
1527

Figure 7. Effect of smoothing and aggregation errors in a high-resolution inversion of methane emissions using SCIAMACHY observations of methane columns for summer 2004. The top left panel shows the correction factors to prior emissions when attempting to optimize emissions at the native $1/2^{\circ} \times 2/3^{\circ}$ grid resolution of the chemical transport model ($n = 7906$). The top right panel shows the same inversion but with a reduced state vector ($n = 1000$) constructed by hierarchical clustering of the native-resolution grid cells (bottom left panel). The bottom right panel shows the ability of the inversion to fit the satellite observations as the state vector dimension is decreased from $n = 7906$ to $n = 3$ by hierarchical clustering. The quality of the fit is measured by the observational terms of the cost function for the inversion. Optimal results are achieved for n in the range 300-1,000. Finer resolution incurs large smoothing errors, while coarser resolution incurs large aggregation errors. Adapted from Wecht et al. (2014a).



1528
1529

1530 Figure 8. Cumulative frequency distribution of spatially resolved annual mean methane
1531 emissions in the contiguous US. The left panel shows the distribution of emissions at $0.1^{\circ}\times 0.1^{\circ}$
1532 resolution in the gridded US EPA inventory for 2012 (Maasakkers et al., 2016). The right panel
1533 shows the distribution of point source emissions in the Greenhouse Gas Reporting Program
1534 (GHGRP) data for 2012. The highest sources are colored by sector. The x-axis is a normal
1535 cumulative probability scale such that a lognormal distribution would plot as a straight line. The
1536 cumulative relative contribution to the national total emissions is shown as the top axis. As an
1537 example of how to read these plots, the top 1% of GHGRP point source emissions (99th quantile
1538 in the right panel) includes $n = 6887/99 = 69$ point sources larger than 1.2 tons h^{-1} and
1539 contributes 71% of total US point source emissions in the GHGRP inventory.
1540